SUPPLEMENTARY INFORMATION

doi:10.1038/nature10915

Contents:

1. Proxy database

1.1 Database

The database used in this study is composed of 80 published high-resolution temperature records derived from alkenones (n=32), planktic foraminiferal Mg/Ca (n=26), microfossil assemblages (n=6), ice-core stable isotopes (n=6), pollen (n=4), TEX_{86} (n=4), and MBT/CBT (n=2) (Table S1). Only records of reasonably high resolution (generally < 500 years) and firm chronological control (generally ≥ 4 radiocarbon dates) were included. Sixty-seven records are dated by radiocarbon, six are ice cores dated by layer counting and/or glaciological modeling, four are dated by a combination of radiocarbon and tuning to layer-counted records, two are entirely tuned to other radiometric chronologies, and one is dated by biostratigraphy.

Table S1. The deglacial proxy temperature database used in this study.

#	Location	Core	Proxy	Reference	Lat (°)	Lon (°)	Elev/Depth (m)	Chronology	Resolution (yr)
1	NGRIP, Greenland	-	ice core $\delta^{18}O$ and borehole temp	Cuffey and Clow, 1997[1]; Andersen et al., 2006[2], Rasmussen et al., 2006[3]	75.1	-42.3	2917	layer counted	20
2	GRIP, Greenland	-	ice core $\delta^{18}O$ and borehole temp	Cuffey and Clow, 1997[1]; Rasmussen et al., 2006[3], 2007[4]	72.6	-37.6	3200	layer counted	20
3	Burial Lake, Alaska	-	chironomids	Kurek et al., 2009[5]	68.4	-159.2	460	^{14}C	352
4	Eastern Beringia (A)	-	pollen	Viau et al., 2008[6]	67.5	-165	-	^{14}C	101
5	Eastern Beringia (B)	-	pollen	Viau et al., 2008[6]	67.5	-137.5	-	^{14}C	101
6	Eastern Beringia (C)	-	pollen	Viau et al., 2008[6]	62.5	-165	-	^{14}C	124
7	Eastern Beringia (D)	-	pollen	Viau et al., 2008[6]	62.5	-137.5	-	^{14}C	101
8	Northeast Atlantic	NA 87-22	foram assemblages	Waelbroeck et al., 2001[7]	55.5	-14.7	-2161	^{14}C and SST tuned to Greenland	246
9	Northeast Atlantic	MD01-2461	Mg/Ca	Peck et al., 2008[8]	51.8	-12.9	-1153	^{14}C and N. pachyderma (s.) %	116

								tuned to Greenland116	
10	California margin	W8709A-8	$U^{K'}_{37}$	Prahl et al., 1995[9]	42.5	-127.7	-3111	^{14}C	620
11	central North Atlantic	CH 69-09	foram assemblages	Waelbroeck et al., 2001[7]	41.8	-47.4	-4100	^{14}C and SST tuned to Greenland	167
12	Japan margin	PC-6	$U^{K'}_{37}$	Minoshima et al., 2007[10]	40.4	143.5	-2215	^{14}C biostratigraphy (foraminiferal ecozones ^{14}C-dated elsewhere)	167
13	Western Mediterranean	BS79-38	$U^{K'}_{37}$	Cacho et al., 2001[11]	38.4	13.6	-1489		155
14	Iberian margin	SU81-18	$U^{K'}_{37}$	Bard et al., 2000[12]	37.8	-10.2	-3135	^{14}C	316
15	Iberian margin	SU81-18	foram assemblages	Waelbroeck et al., 2001[7]	37.8	-10.2	-3135	^{14}C benthic $\delta^{18}O$ tuned to ^{14}C-dated core SU90/08	234
16	North Atlantic	MD95-2037	$U^{K'}_{37}$	Calvo et al., 2001[13]	37.1	-32.0	-2630		484
17	Gulf of Cadiz	M39-008	$U^{K'}_{37}$	Cacho et al., 2001[11]	36.4	-7.1	-576	^{14}C	113
18	Alboran Sea	MD95-2043	$U^{K'}_{37}$	Cacho et al., 1999[14]	36.1	-2.6	-1841	^{14}C	152
19	North Pacific	MD01-2421	$U^{K'}_{37}$	Isono et al., 2009[15]	36	141.8	-2224	^{14}C loess proxy records tuned to ^{230}Th-dated Hulu/Sanbao Cave speleothems	246
20	Chinese loess plateau	Section MS2008E	MBT/CBT	Peterse et al., 2011[16]	34.9	113.3	~200		397
21	Bermuda Rise	OCE326-GGC5	Mg/Ca	Carlson et al., 2008[17]	33.7	-57.6	-4550	^{14}C	408
22	Japan margin	KT92-17 St. 14	$U^{K'}_{37}$	Sawada and Handa, 1998[18]	32.6	138.6	-3252	^{14}C	443
23	Blake outer ridge	KNR140-51GGC	Mg/Ca	Carlson et al., 2008[17]	32.6	-76.3	-1790	^{14}C	397
24	Nile Delta	GeoB 7702-3	TEX_{86}	Castañeda et al., 2010[19]	31.7	34.1	-562	^{14}C	316
25	Japan margin	KY07-04-01	Mg/Ca	Kubota et al., 2010[20]	31.6	128.9	-758	^{14}C	115
26	East China Sea	MD98-2195	$U^{K'}_{37}$	Ijiri et al., 2005[21]	31.6	129	-746	^{14}C	165
27	Gulf of Mexico	MD02-2575	Mg/Ca	Ziegler et al., 2008[22]	29.0	-87.1	-847	^{14}C	282
28	Red Sea	GeoB 5844-2	$U^{K'}37$	Arz et al., 2003[23]	27.7	34.7	-963	^{14}C	316
29	Gulf of Mexico	EN32-PC6	Mg/Ca	Flower et al., 2004[24]	27.0	-91.3	-2280	^{14}C	185
30	Northwest African margin	ODP 658C	foram assemblages	deMenocal et al., 2000[25]	20.8	-18.6	-2263	^{14}C	176
31	Northwest African margin	ODP 658C	$U^{K'}_{37}$	Zhao et al., 1995[26]	20.8	-18.6	-2263	^{14}C	115
32	South China Sea	17940	$U^{K'}_{37}$	Pelejero et al., 1999[27]	20.1	117.4	-1968	^{14}C	161
33	South China Sea	ODP 1144	Mg/Ca	Wei et al, 2007[28]	20.1	117.6	-2037	^{14}C	337
34	Arabian Sea	74KL	$U^{K'}_{37}$	Huguet et al., 2006[29]	14.3	57.3	-3212	^{14}C	304
35	Arabian Sea	74KL	TEX_{86}	Huguet et al., 2006[29]	14.3	57.3	-3212	^{14}C	310
36	Western tropical North Atlantic	M35003-4	$U^{K'}_{37}$	Rühlemann et al., 1999[30]	12.1	-61.3	-1299	^{14}C	344
37	Western Caribbean Sea	VM28-122	Mg/Ca	Schmidt et al., 2004[31]	11.6	-78.4	-3623	^{14}C	352
38	Arabian Sea	NIOP-905	$U^{K'}_{37}$	Huguet et al., 2006[29]	10.8	51.9	-1567	^{14}C	204
39	Arabian Sea	NIOP-905	TEX_{86}	Huguet et al., 2006[29]	10.8	51.9	-1567	^{14}C	204
40	Cariaco Basin, Venezuala	PL07-39PC	Mg/Ca	Lea et al., 2003[32]	10.7	-65.0	-790	^{14}C and grayscale tuned to varved core 56PC	110
41	Sulu Sea	MD97-2141	Mg/Ca	Rosenthal et al., 2003[33]	8.8	121.3	-3633	^{14}C	78
42	Eastern equatorial Pacific	MD02-2529	$U^{K'}_{37}$	Leduc et al., 2007[34]	8.2	-84.1	-1619	^{14}C	282
43	Eastern equatorial Pacific	ME0005A-43JC	Mg/Ca	Benway et al., 2006[35]	7.9	-83.6	-1368	^{14}C	207
44	South China Sea	MD01-2390	$U^{K'}_{37}$	Steinke et al., 2008[36]	6.6	113.4	-1545	^{14}C	287
45	South China Sea	MD01-2390	Mg/Ca	Steinke et al., 2008[36]	6.6	113.4	-1545	^{14}C	221
46	West Pacific warm pool	MD98-2181	Mg/Ca	Stott et al., 2007[37]	6.3	125.8	-2114	^{14}C	56
47	Gulf of Guinea	MD03-2707	Mg/Ca	Weldeab et al., 2007[38]	2.5	9.4	-1295	^{14}C	90
48	Eastern equatorial Atlantic	GeoB 4905	Mg/Ca	Weldeab et al,. 2005[39]	2.5	9.4	-1328	^{14}C	180
49	Eastern equatorial Pacific	TR163-22	Mg/Ca	Lea et al., 2006[40]	0.5	-92.4	-2830	^{14}C	242
50	Eastern equatorial Pacific	ME0005A-24JC	$U^{K'}_{37}$	Kienast et al., 2006[41]	0.0	-86.5	-2941	^{14}C	209
51	Eastern equatorial Pacific	V21-30	$U^{K'}_{37}$	Koutavas and Sachs, 2008[42]	-1.2	-89.7	-617	^{14}C	360
52	Eastern equatorial Pacific	V21-30	Mg/Ca	Koutavas et al., 2002[43]	-1.2	-89.7	-617	^{14}C	408
53	Eastern equatorial Pacific	V19-28	$U^{K'}_{37}$	Koutavas and Sachs, 2008[42]	-2.4	-84.7	-2720	^{14}C	596
54	Brazilian margin	GeoB 3910	$U^{K'}_{37}$	Jaeschke et al., 2007[44]	-4.2	-36.3	-2362	^{14}C	221
55	Western tropical Atlantic	GeoB 3129	Mg/Ca	Weldeab et al, 2006[45]	-4.6	-36.6	-830	^{14}C	112
56	West Pacific warm pool	MD9821-62	Mg/Ca	Visser et al., 2003[46]	-4.7	117.9	-1855	^{14}C	323
57	West Pacific warm pool	MD98-2176	Mg/Ca	Stott et al., 2007[37]	-5.0	133.4	-2382	^{14}C	119

58	Gulf of Guinea	GeoB 6518-1	MBT/CBT	Weijers et al., 2007[47]	-5.6	11.2	-962	^{14}C	189
59	Gulf of Guinea	GeoB 6518-1	$U^{K'}_{37}$	Schefuß et al., 2005[48]	-5.6	11.2	-962	^{14}C	204
60	Lake Tanganyika	NP04-KH3, KH4	TEX_{86}	Tierney et al., 2008[49]	-6.7	29.6	773	^{14}C	221
61	West Pacific warm pool	MD98-2165	Mg/Ca	Levi et al., 2007[50]	-9.7	118.4	-2100	^{14}C	176
62	West Pacific warm pool	MD98-2170	Mg/Ca	Stott et al., 2007[37]	-10.6	125.4	-832	^{14}C	369
63	Timor Sea, Indian Ocean	MD01-2378	Mg/Ca	Xu et al., 2008[51]	-13.1	121.8	-1783	^{14}C	131
64	Southeast Atlantic	GeoB 1023-5	$U^{K'}_{37}$	Kim et al., 2002[52]	-17.2	11.0	-1978	^{14}C	97
65	Indian Ocean	MD79257	$U^{K'}_{37}$	Bard et al., 1997[53]	-20.4	36.3	-1260	^{14}C	282
66	Subtropical southeast Atlantic	ODP 1084B	Mg/Ca	Farmer et al., 2005[54]	-25.5	13.0	-1992	^{14}C	91
67	Brazilian margin	KNR159-5-36GGC	Mg/Ca	Carlson et al., 2008[17]	-27.5	-46.5	-1268	^{14}C	484
68	Chilean margin	GeoB 7139-2	$U^{K'}_{37}$	Kaiser et al., 2005[55]	-30.2	-72.0	-3270	^{14}C	330
69	South Australia	MD03-2611	$U^{K'}_{37}$	Calvo et al., 2007[56]	-36.7	136.7	-2420	^{14}C	344
70	New Zealand	MD97-2121	$U^{K'}_{37}$	Pahnke and Sachs, 2006[57]	-40.4	178.0	-3014	^{14}C	84
71	Chilean margin	ODP 1233	$U^{K'}_{37}$	Lamy et al., 2007[58]	-41.0	-74.5	-838	^{14}C	112
72	Southeast Atlantic	TN057-21-PC2	$U^{K'}_{37}$	Sachs et al., 2001[59]	-41.1	7.8	-4981	^{14}C	110
73	Southeast Atlantic	TN057-21	Mg/Ca	Barker et al., 2009[60]	-41.1	7.8	-4981	^{14}C	168
74	New Zealand	SO136-GC11	$U^{K'}_{37}$	Barrows et al., 2007[61]	-43.5	167.9	-1556	^{14}C	194
75	New Zealand	MD97-2120	$U^{K'}_{37}$	Pahnke and Sachs, 2006[57]	-45.5	174.9	-1210	^{14}C	122
76	Southern Ocean	MD88-770	foram assemblages	Labeyrie et al., 1996[62]	-46.0	96.5	-3290	^{14}C	218
77	EDML, Antarctica	-	ice core $\delta^{18}O$	Stenni et al., 2010[63]; Lemieux-Dudon et al., 2010[64]	-75	0	2892	glaciological model and stratigraphic constraints	103
78	Dome C, Antarctica	-	ice core $\delta^{18}O$	Stenni et al., 2010[63]; Lemieux-Dudon et al., 2010[64]	-75.1	123.4	3240	glaciological model and stratigraphic constraints	103
79	Dome Fuji, Antarctica	-	ice core $\delta^{18}O$, δD	Kawamura et al., 2007[65]	-77.3	39.7	3810	glaciological model	500
80	Vostok, Antarctica	-	ice core δD	Petit et al., 1999[66]	-78.5	108.0	3500	glaciological model	62

1.2 Data density

A total of ~8400 proxy temperature measurements and 636 radiocarbon dates among the 80 records lie within the interval 22-6.5 ka (Figure S1a,b). The median resolution of the records is 200 years (Figure S2). All 80 records span 18-11 ka and ~85% span 22-6.5 ka (Figure S1c).

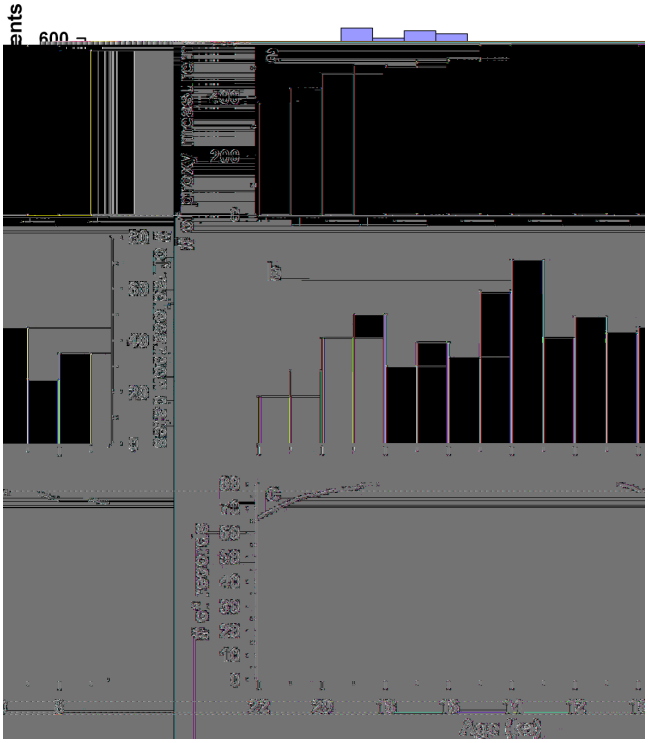

Figure S1: Data density. Distribution of (**a**) proxy temperature measurements, (**b**) radiocarbon dates, and **(c)** proxy records through time.

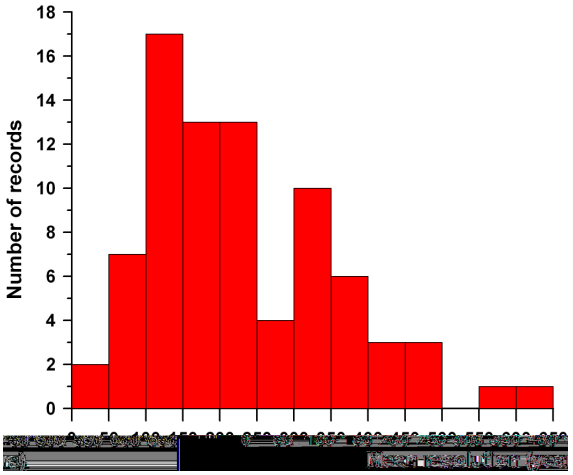

Figure S2: Histogram of the mean resolution of the proxy records from 22-6.5 ka.

2. Age control

The three most common types of age control used in this synthesis are radiocarbon ages, Greenland layer counts, and Antarctic timescales. We discuss each and their uncertainties here.

2.1 Radiocarbon ages

Most of the non-ice core records are either directly or indirectly tied into radiocarbon chronologies. Radiocarbon-based age models have three main sources of uncertainty: (1) marine reservoir correction uncertainties, (2) errors on calibrated radiocarbon dates, and (3) interpolating age models between dates. The latter two were explicitly accounted for in our Monte Carlo simulations.

(1) We applied the reservoir corrections used by the original authors, which average 463 years over the 19-6 ^{14}C ka interval (Figure S3). Reservoir corrections were assumed to be 400 years if not otherwise stated in the original publications. Assuming larger (smaller) reservoir corrections would shift the temperature stack younger (older).

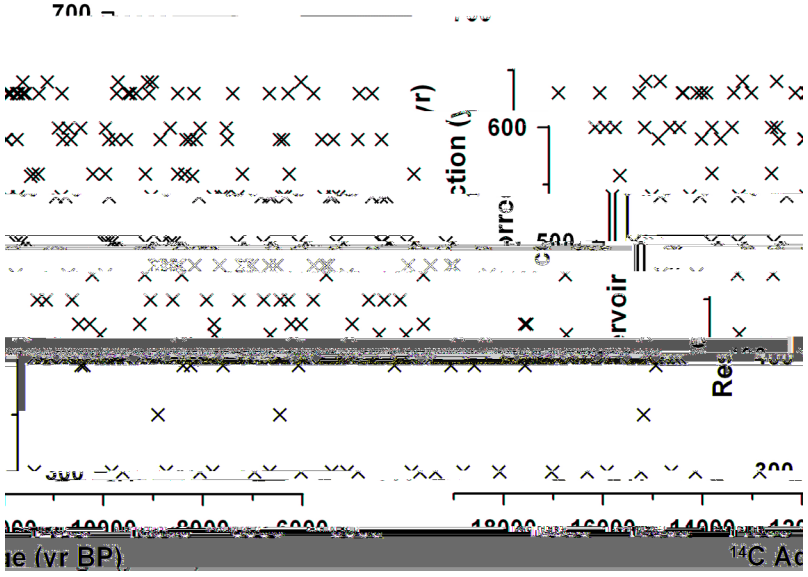

Figure S3: Radiocarbon reservoir corrections for all dates from the 62 radiocarbon-dated marine records in the database, as suggested by the original authors.

One way to check the reasonableness of the applied reservoir corrections is to compare climate signals in marine and terrestrial records, since terrestrial archives generally do not suffer from radiocarbon reservoir issues. Clark et al.[67] recently calculated the two leading modes of deglacial temperature variability from a global proxy dataset using empirical orthogonal function analysis. Dividing the dataset into land (n=53) and ocean (n=74) records yields similar leading modes of variability (r^2=0.98 and 0.80 for principal components 1 and 2), suggesting that the two realms record the same climate signals (Figure S4). Lag correlations suggest the ocean modes are 300 years older than the land modes, however, which may imply reservoir corrections have been underestimated. Similar logic can be applied to upwelling versus non-upwelling regions in the ocean to investigate reservoir corrections, since reservoir ages are expected to be more variable at upwelling sites. The two leading modes of variability for calibrated sea surface temperature records from upwelling (n=19) and non-upwelling (n=50) areas appear to be reversed, such that non-upwelling PC1 correlates with upwelling PC2 (r^2=0.93) and non-upwelling PC2 correlates with upwelling PC1 (r^2=0.81), indicating that the millennial variability mode is more important at upwelling sites while the overall deglacial warming mode dominates at non-upwelling sites (Figure S4). Nonetheless, the strong correlations of these climate modes suggest that the two domains may record the same signals. Lag correlations suggest the upwelling modes are older than the non-upwelling modes by 300 and 200 years, which again may imply underestimated marine reservoir corrections. These observations therefore imply that, if anything, errors in reservoir corrections might shift the global temperature stack slightly younger, increasing its lag behind atmospheric CO_2.

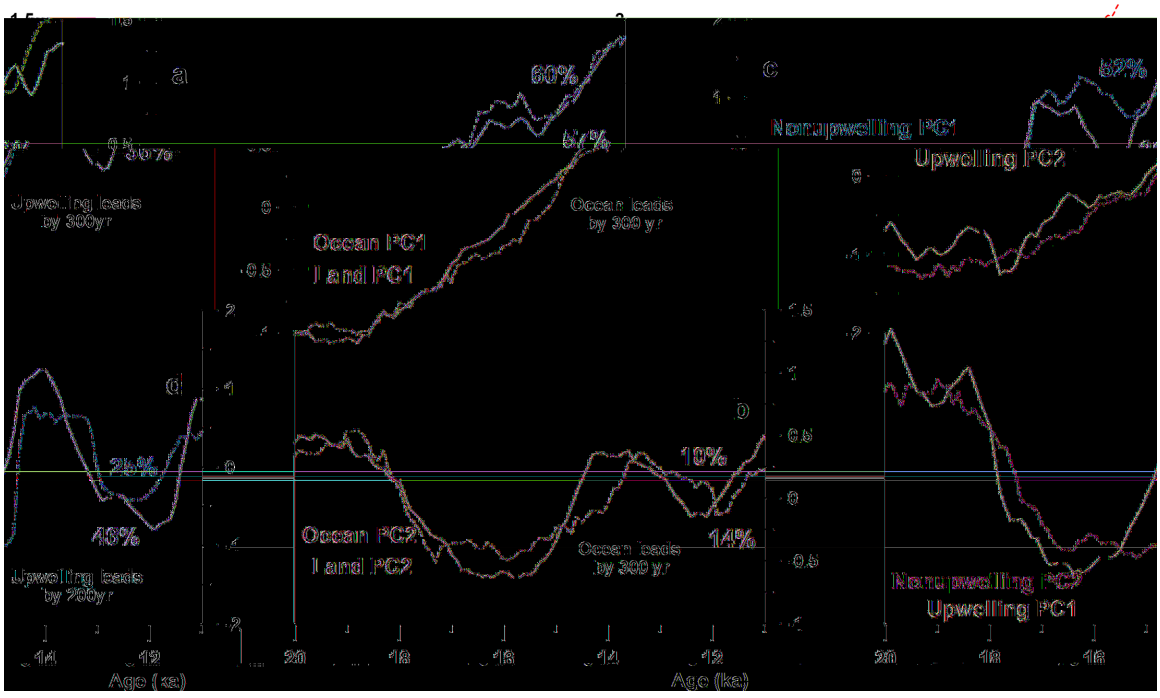

Figure S4: Leading principal components (PC) of deglacial temperatures variability. (**a,b**) land and ocean sites. (**c,d**) upwelling and non-upwelling sites in the ocean. The fraction of variance explained by the modes and their relative timing as determined from lag correlations are given. (adapted from Clark et al.[67])

(2) All dates were recalibrated with Calib 6.0.1 using the IntCal04 calibration. To simplify the often non-Gaussian errors on calibrated radiocarbon dates, we treated the upper and lower 2σ calibrated ages as a Gaussian 2σ uncertainty about a centered mean age in the Monte Carlo simulations. Age models were then allowed to vary within these uncertainties at the depths of the radiocarbon dates.

(3) Between radiocarbon dates, we used a random walk model[68] that allows age models to "jitter" more the further they are from a radiocarbon date. To determine a reasonable jitter value (J) we used the existing radiocarbon dates in the database between 10 and 20 ka and calculated the deviation of a date from its expected (i.e., linear) age between two bounding dates. This procedure was repeated for all possible permutations of dates, yielding 3769 values of J (Figure S5). We used the median J value (J = 188) to

perturb the radiocarbon-based age models with autocorrelated errors in our Monte Carlo analysis. Age models and their estimated uncertainties are shown in Appendix S1.

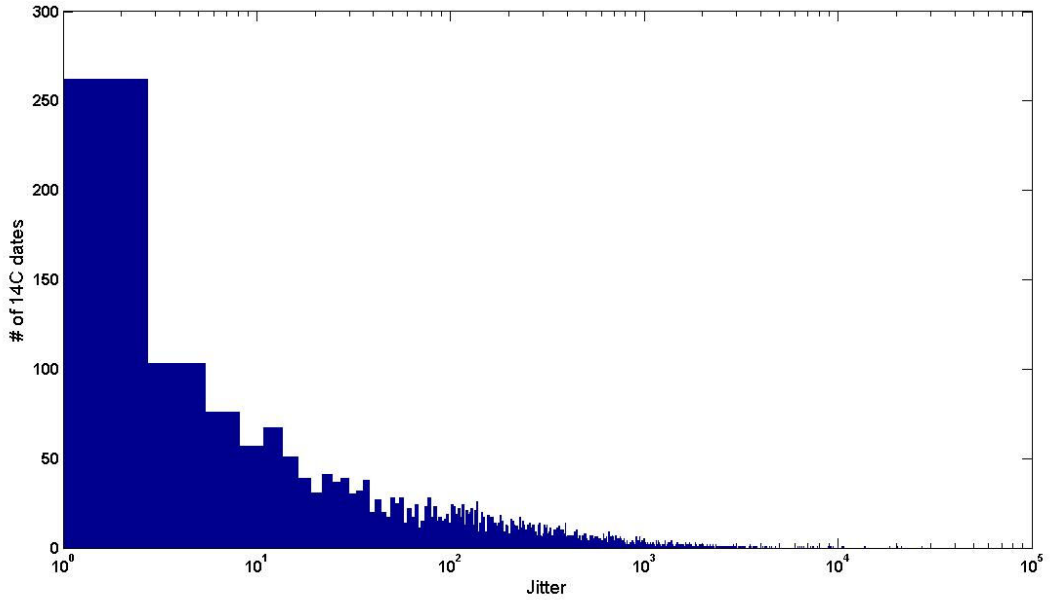

Figure S5: Histogram of 3769 age model jitter values calculated from radiocarbon data from 20-10 ka, as described in the text. The median jitter value is 188.

A final uncertainty related to radiocarbon dating is the calibration, which is discussed below in Section 5.5.

2.2 Greenland layer counting

The NGRIP and GRIP ice cores are anchored by the layer-counted GICC05 timescale, and four other marine records are tuned to earlier layer-counted Greenland timescales. GICC05 appears to be fairly well linked into the radiocarbon timescale during the deglaciation[69]. Maximum counting errors for GICC05 suggest that absolute age uncertainty (1σ) increases from approximately 10 to 265 years over our 6.5-22 ka study interval (≤ 1.2% errors) (refs. 3,70). Our Monte Carlo simulations used these time-varying uncertainties for the NGRIP and GRIP ice cores, and assumed 2% uncertainties for the records tuned to Greenland.

2.3 Antarctic timescales

The EDC and EDML ice cores have been synchronized with Greenland by Lemieux-Dudon et al.[64], and we use their time-varying error estimates, which approach nearly 400 years (2σ) at the onset of deglaciation. Pedro et al.[71] suggest a similar uncertainty for their composite Antarctic record based on five ice cores at the onset of deglaciation. The age models of the Dome F and Vostok ice cores are based on glaciological flow models, and we assume 2% (1σ) errors.

Critical to our analysis is the age model and uncertainty for the atmospheric CO_2 record. We used EDC CO_2, which was recently placed on an improved timescale based on a best compromise between glaciological modeling and ice and gas stratigraphic constraints among several Antarctic and Greenland ice cores by Lemieux-Dudeon et al.[64]. Because Lemieux-Dudon et al.[64] did not quantify gas age uncertainties, however, we estimated chronological uncertainties for the CO_2 record based on the errors associated with CH_4 synchronization of EDC with Greenland. There are three sources of uncertainty in this process that we account for. First, the Greenland ice-age timescale (GICC05) is derived from annual layer counting of the NGRIP ice core. Andersen et al.[70] and Rasmussen et al.[3] provide "maximum counting errors" associated with this process, which Andersen et al. suggest regarding as 2σ uncertainties. Second, transferring the GICC05 ice age timescale to the Greenland composite CH_4 record[72] requires knowledge of Greenland ice age-gas age differences, or delta ages. A rigorous assessment of delta age uncertainty does not exist in the literature. We therefore considered delta age uncertainty to be 20% of delta age itself, an estimate that we regard as conservative. In actuality, delta age is precisely known during the abrupt onsets of the Bølling, Younger

Dryas, and Holocene periods, when nitrogen and argon isotopes indicate CH_4 and Greenland ice $\delta^{18}O$ variations were nearly synchronous[73]. Third, CH_4 concentration errors introduce uncertainty during tuning of EDC CH_4 to the Greenland composite CH_4 record. We estimated this uncertainty with 1000 Monte Carlo simulations in which the two CH_4 records were randomly perturbed with 10 ppbv errors (1σ) and tuned using the program XCM[68]. To provide a conservative estimate of the combined uncertainty due to these three sources of error, we added them arithmetically (Figure S6).

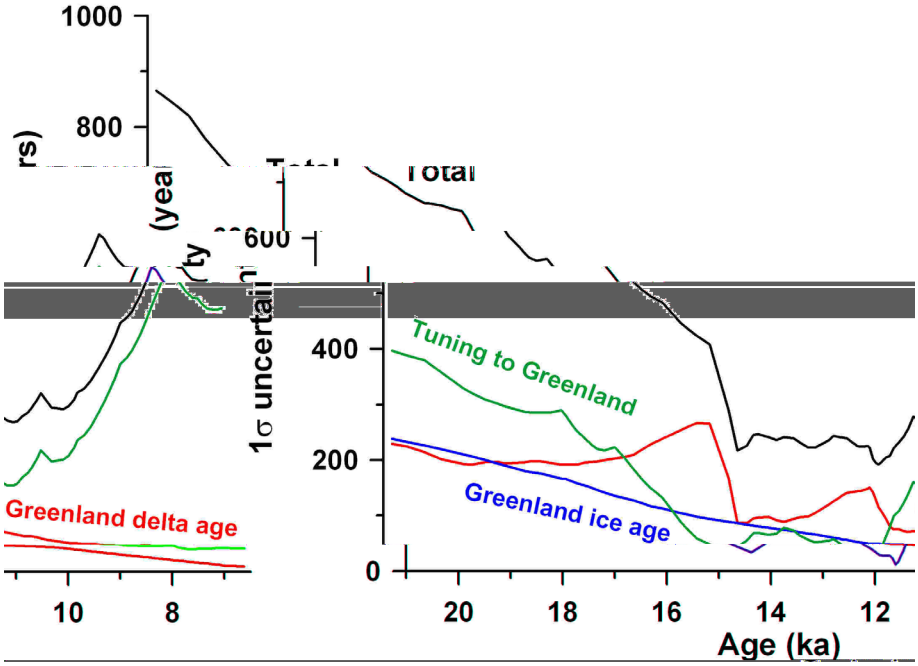

Figure S6: CO_2 age-model uncertainty. Total age uncertainty in the EDC CO_2 record over the last deglaciation associated with methane-synchronization to Greenland (black), which reflects the sum of uncertainties associated with Greenland ice ages (blue), Greenland ice age-gas age differences (red), and tuning EDC and Greenland CH4

To further examine the robustness of the Lemieux-Dudon et al.[64] EDC gas chronology, we compared it to GICC05. EDC CH_4 tuned to GICC05 is generally older than on the Lemieux-Dudon et al.[64] timescale, and this offset is particularly evident at the Bølling onset (Figure S7b). Greenland composite CH_4 and NGRIP $\delta^{18}O$ on Lemieux-

Dudon et al.[64] exhibit a similar offset at the Bølling onset (Figure S7a). Since abrupt Greenland warmings are known to be synchronous with CH_4 jumps[73], this offset likely reflects an error in the Lemieux-Dudon et al.[64] gas chronology, which if corrected would shift the EDC CO_2 record a couple centuries older at the Bølling (Figure S7c). A similar though smaller offset seems to occur at the Younger Dryas while no offset exists at the Holocene onset (Figure S7d). The lack of structure in the CH_4 record at the onset of deglaciation makes it difficult to precisely determine the timing of the initial CO_2 rise, which is reflected in the larger error bars at this time (Figure S6).

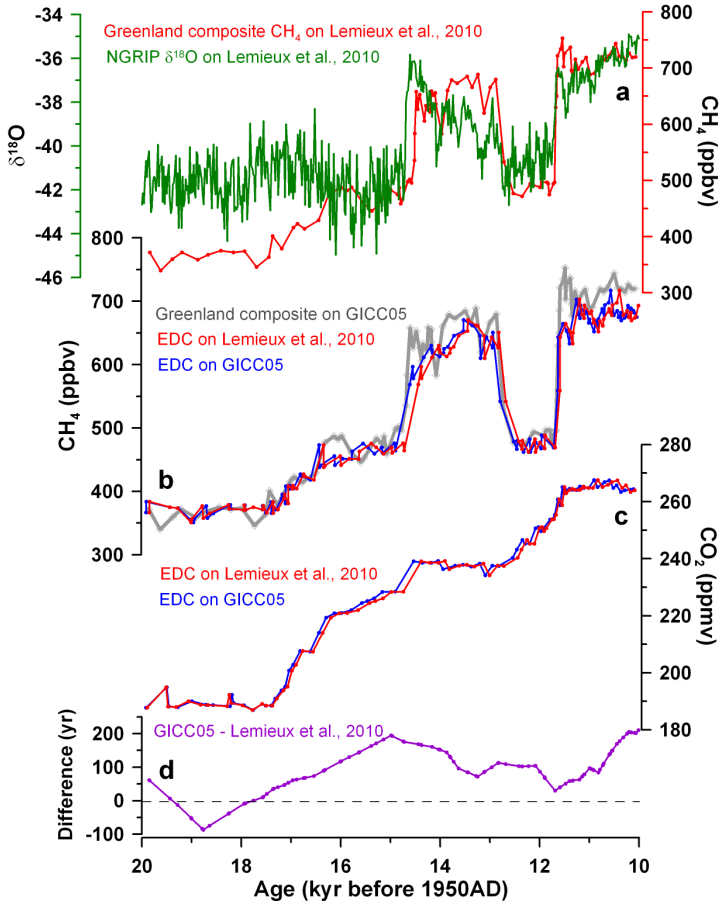

Figure S7: Ice core age models. (**a**) Greenland composite CH_4 and NGRIP $\delta^{18}O$ on the Lemieux-Dudon et al.[64] timescale. (**b**) Greenland composite CH_4 on the GICC05 timescale and EDC CH_4 on the Lemieux-Dudon et al.[64] and GICC05 timescales. (**c**) EDC CO_2 on the Lemieux-Dudon et al.[64] and GICC05 timescales. (**d**) Difference between the Lemieux-Dudon et al.[64] and GICC05 gas timescales.

3. Monte Carlo simulations

We used Monte Carlo simulations to generate 1000 realizations of each proxy temperature record, and the global temperature stack in turn. An example record is shown in Figure S8. First, continuous age-model uncertainty estimates were calculated for each record as explained above in Section 2.1 (Figure S8a). 1000 age models were then generated for each record by perturbing its chronology with autocorrelated errors using these uncertainty estimates (Figure S8b). Age models were linearly extrapolated beyond the top and bottommost dates in a core using the mean sedimentation rate over the dated interval of the core. Next, the proxy values were converted to temperature 1000 times, perturbing the temperature calibration with the errors given in the Methods section of the paper (Figure S8c); temperature errors were assumed to be random in time and space. These perturbed proxy temperature records were then linearly interpolated onto the perturbed age models at 100-year resolution and converted to anomalies from the early Holocene (11.5-6.5 ka) mean to yield 1000 realizations of each record (Figure S8d). Lastly, the first realizations of the 80 records were stacked, followed by the second, third, fourth, etc., generating 1000 realizations of the global temperature stack (Figure S9). The temperature stack and error bars shown in the main paper are the mean and standard deviation of these 1000 realizations. Temperature records and their estimated uncertainties are shown in Appendix S2. The analytical code used in this study will be published in Marcott et al.[74].

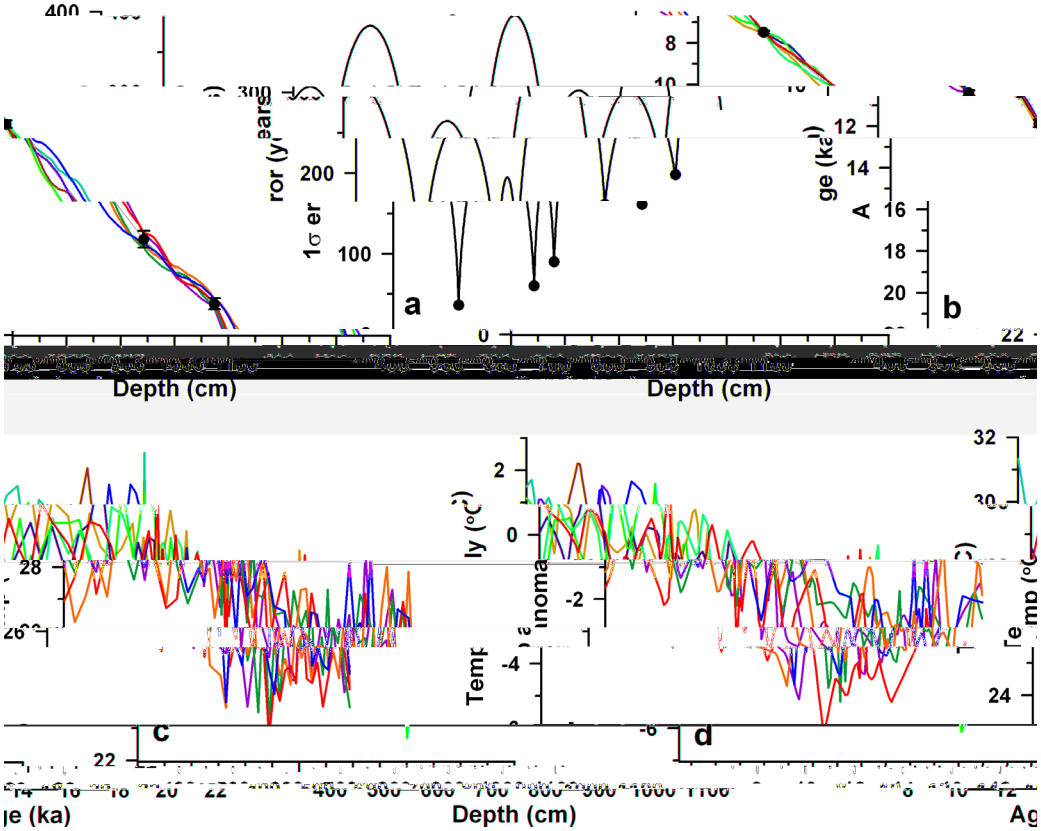

Figure S8: Example of five Monte Carlo simulations with the Visser et al.[46] West Pacific Warm Pool Mg/Ca record. (**a**) Estimated age model error. Black dots show the locations of radiocarbon dates. (**b**) Perturbed age models. Black dots and error bars show radiocarbon dates. (**c**) Perturbed temperature records. (**d**) Perturbed temperature records linearly interpolated onto the perturbed age models at 100-year resolution and referenced as anomalies from the early Holocene (11.5-6.5 ka) mean.

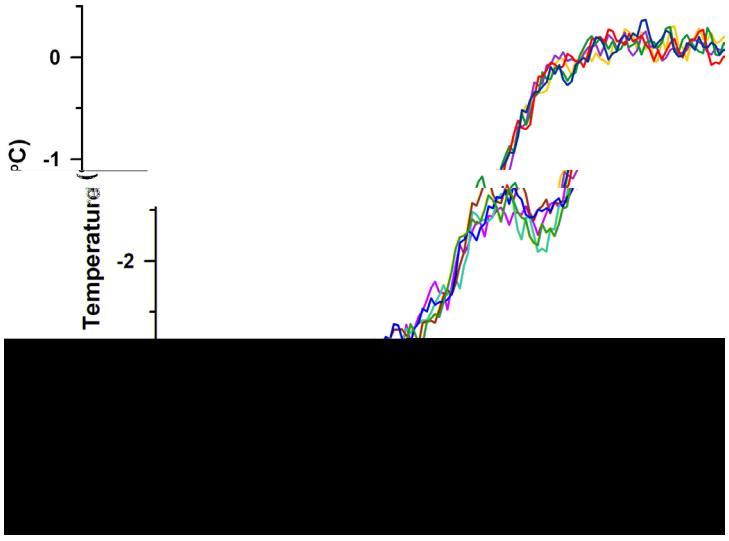

Figure S9: Five realizations of the global temperature stack, derived from perturbing the proxy records with chronological and temperature calibration errors.

The standard deviation of the 1000 global temperature stacks provides a measure of the propagated error due to chronological and temperature uncertainties in the individual records (Figure S10). We performed this Monte Carlo procedure including only temperature uncertainties, only chronological uncertainties, and both temperature and chronological uncertainties. We find that error in the temperature stack due to chronological uncertainties generally increases with age, as expected, though there are local maxima in error at times of large temperature shifts, such as the onsets of the deglaciation, Bølling/Allerød, Younger Dryas, and Holocene. Errors associated with temperature uncertainties are constant through time, as would also be expected. Temperature uncertainties generally contribute substantially more error to the temperature stack than chronological uncertainties. Tests indicate that errors are proportional to $n^{-½}$, where n is the number of proxy records.

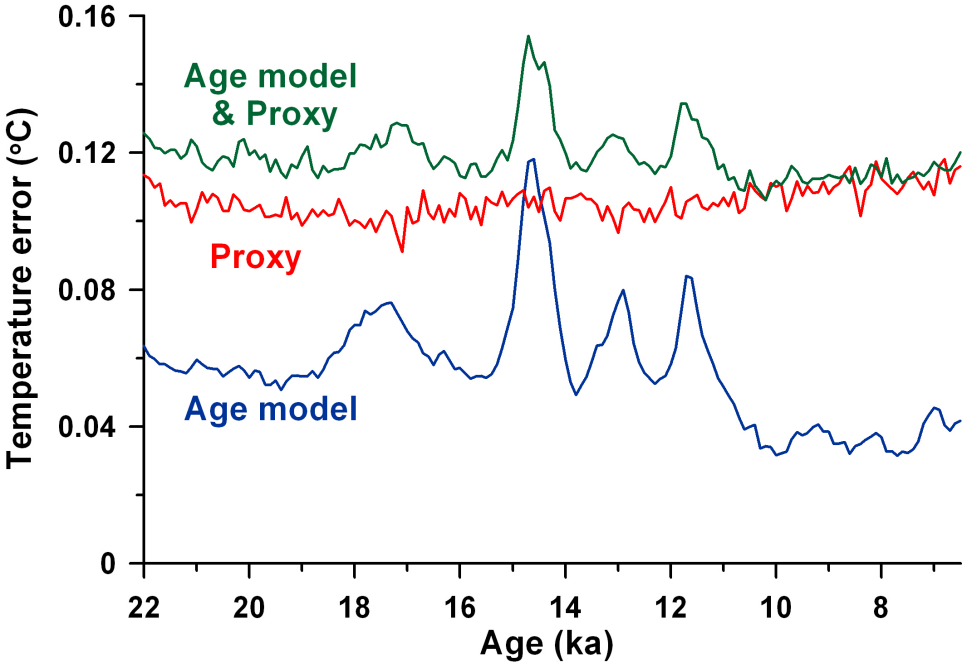

Figure S10: Global temperature stack uncertainties. 1σ error on the global proxy temperature stack due to uncertainties in the age models of the records (blue), the conversion of proxy values to temperature (red), and both (green).

4. How well do the proxy sites represent the globe?

An important assumption of our study is that the 80 proxy records used provide a reasonable representation of global temperature variability. We evaluated this assumption using the instrumental temperature record as well as output from our transient modeling of the last deglaciation.

4.1 Instrumental record

We sampled the 5x5-degree NCDC instrumental blended land and ocean surface temperature dataset from 1880-2007 A.D.[75] at 80 random locations 1000 times to generate 1000 realizations of global mean temperature. The standard deviation of these realizations is 4.5 times smaller than the standard deviation of 20th century global temperature suggesting 80 random points represents the globe reasonably well (Figure S11a). In addition, the mean at the locations of the deglacial proxy records is similar to the true global mean (r^2=0.83), indicating these particular locations faithfully capture the global signal. Repeating this procedure for 67 ocean-only sites (i.e., the number of ocean proxy records) with the 1x1-degree HadISST1 dataset from 1870-2007 A.D.[76] yields similar results (Figure S11b).

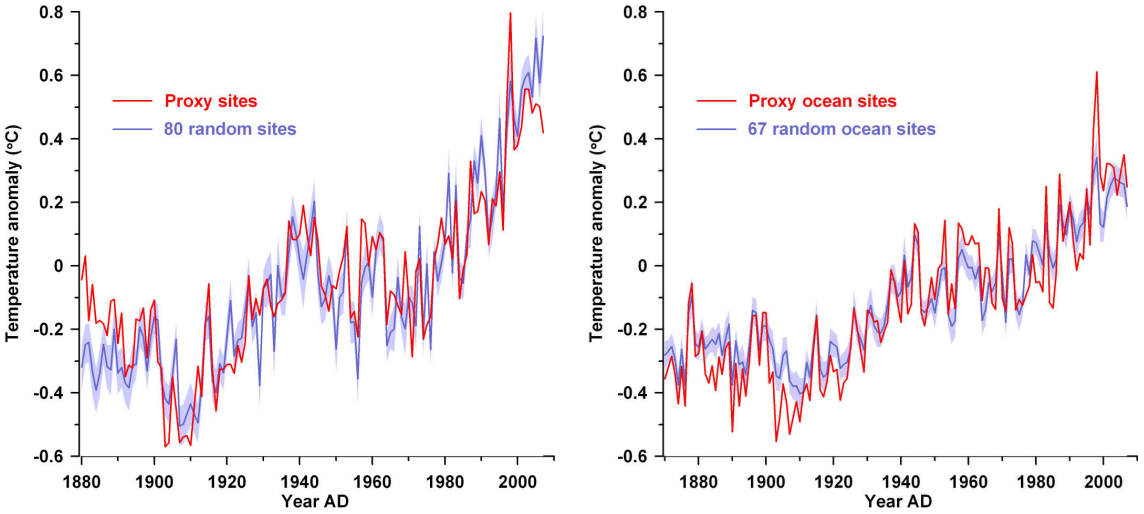

Figure S11: 20th century temperatures at the proxy sites. (a) The mean (blue line) and standard deviation (blue error window) of 1000 realizations of global mean temperature based on a random sampling of 80 locations from the NCDC blended land and ocean dataset (this is equivalent to the true global mean)[75]. Mean temperature at the locations of the 80 deglacial proxy sites (red). **(b)** Same as (a), except confined to the ocean and using the HadISST1 dataset[76].

4.2 Transient deglacial model output

We also compared the mean temperature at the 80 proxy sites in our deglacial model to the global and hemispheric means in the model. The temporal structures of the proxy site means and full-field means are all similar, but while the glacial-interglacial amplitude is accurately represented by the proxy sites in the Southern Hemishere, it is underestimated by ~1°C in the Northern Hemisphere (Figure S12).

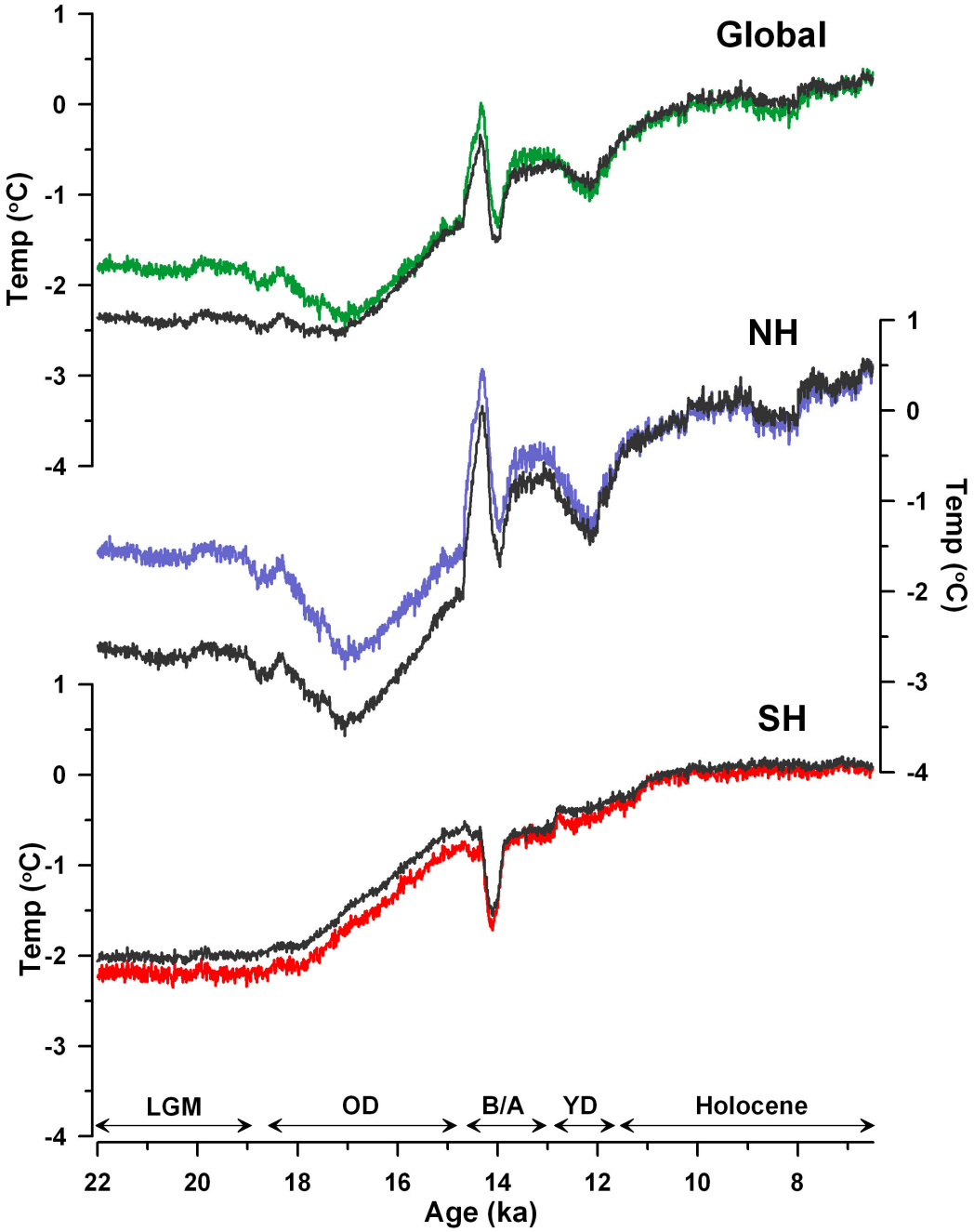

Figure S12: Simulated temperature stacks versus full-field mean temperatures. The mean temperatures in the model for the (**top**) globe, (**middle**) Northern Hemisphere, (**bottom**) and Southern Hemisphere (black), and the area-weighted means in the model at the 80 proxy sites (colored). Sea surface temperatures are used over ocean and surface air temperatures are used over land.

5. How robust is the temperature stack?

We investigate the sensitivity of the proxy temperature stack to several variables including interpolation resolution, areal weighting, the number and type of proxy records, missing data, and radiocarbon calibration.

5.1 Resolution

Recalculating the global temperature stack at 500-year resolution yields an essentially identical stack and error bars, albeit at lower resolution (Figure S13). This is because our uncertainty estimate for global temperature at any given point in time is the standard deviation of 1000 realizations of the global temperature anomaly at that point derived from perturbing the individual records with errors, linearly interpolating to constant resolution, and stacking. So, for example, 500-year resolution results in 1000 global temperature estimates at 11 and 11.5 ka. 100-year resolution yields the exact same results for 11 and 11.5 ka, as well as 1000 temperature estimates at 11.1, 11.2, 11.3, and 11.4 ka that are generally in between those at 11 and 11.5 ka due to the linear interpolation.

We also recalculated the stack using only the records with better than 200-year resolution (n=39; 23 in Northern Hemisphere, 16 in Southern Hemisphere). This stack is, in general, similar, though there is greater overall warming and a larger Younger Dryas cooling (Figure S14).

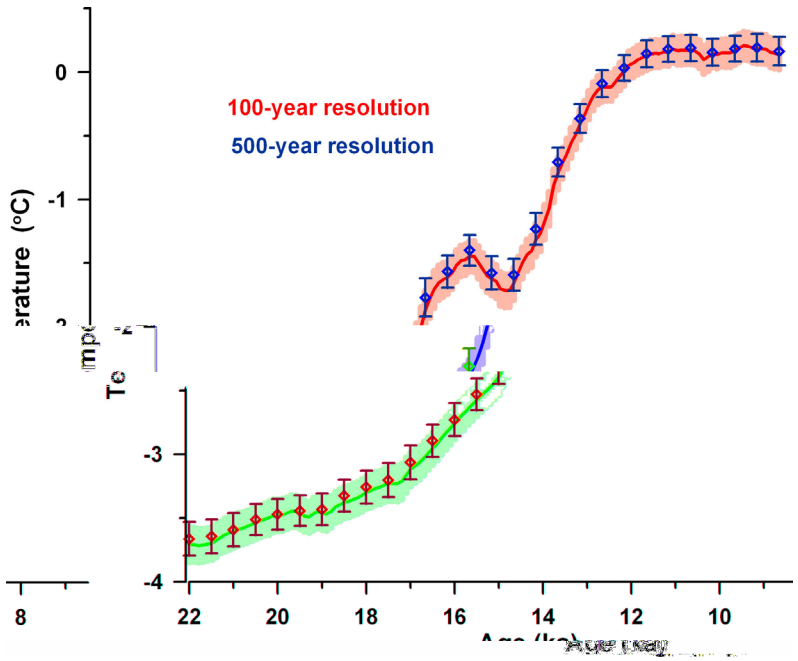

Figure S13: The global temperature stack based on proxy records interpolated to 100-year and 500-year resolution. Errors (1σ) reflect age-model and temperature calibration uncertainty.

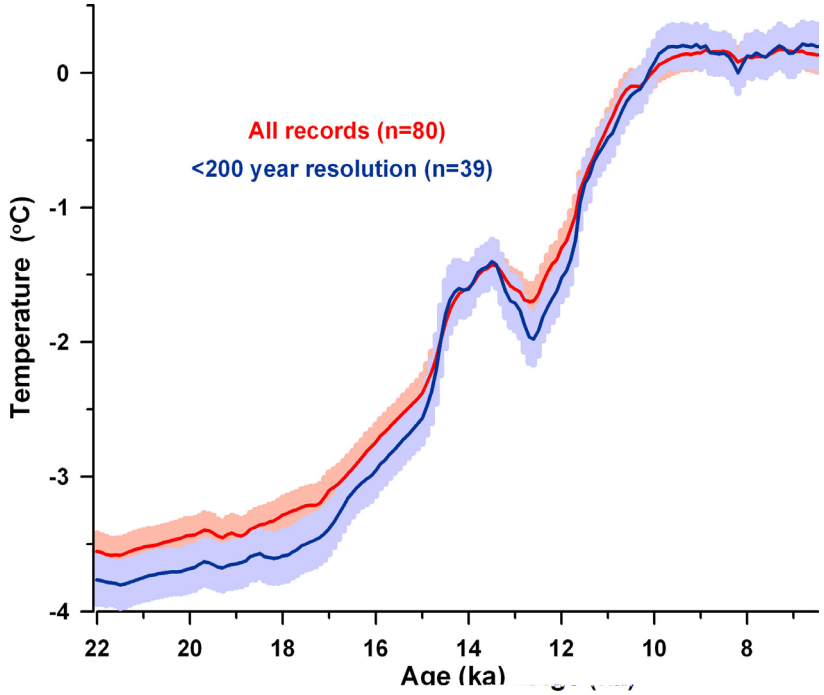

Figure S14: The global temperature stack based on all records and only the records with higher than 200-year resolution. Errors (1σ) reflect age-model and temperature calibration uncertainties.

5.2 Areal weighting

To test the sensitivity of the global temperature stack to areal weighting we show the results of three different schemes here: (1) the area-weighted 5° x 5° gridded average we use in the main paper; (2) the unweighted raw average of the records; (3) a meridional weighting in which the records are first averaged in 10° latitude bands and then stacked weighting by latitude-band area; latitude bands without records were represented by the adjacent latitude band with data. These three stacks have similar temporal structures (Figure S15), suggesting the correlation and phasing of temperature and CO_2 we report is not strongly sensitive to areal weighting. The amplitudes of the stacks differ by up to 15%, however, implying the spatial bias of our dataset affects its ability to constrain the magnitude of glacial cooling.

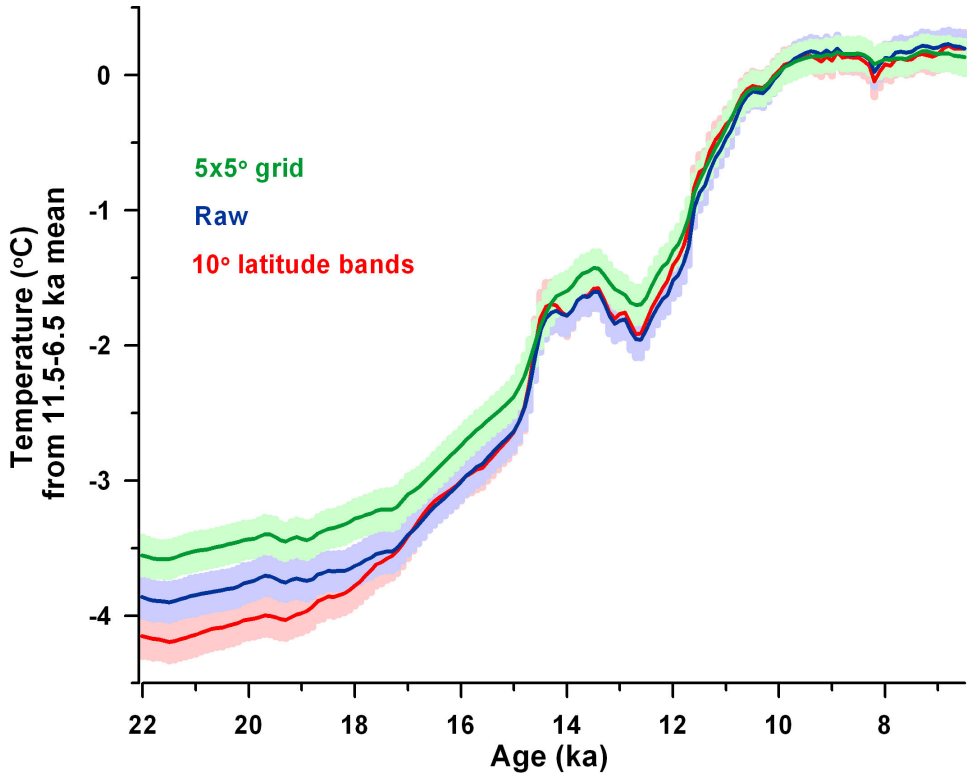

Figure S15: The global temperature stack based on various area-weighting schemes of the data. Errors (1σ) reflect age-model and temperature calibration uncertainties.

5.2 Jackknifing

We used a jackknifing approach to examine the sensitivity of the temperature stack to the number of records used. The stack was recalculated 1000 times after randomly excluding 50% of the records each time. This procedure was also repeated excluding 90% of the records. Note that because the records were perturbed with chronological and proxy errors before jackknifing, the results include these sources of uncertainty. The standard deviation of the jackknifed stacks, particularly for the 50% case, are relatively modest in comparison to the variability in the proxy stack (Figure S16), which suggests the stack is fairly robust and unlikely to change dramatically with the inclusion of more records in the future.

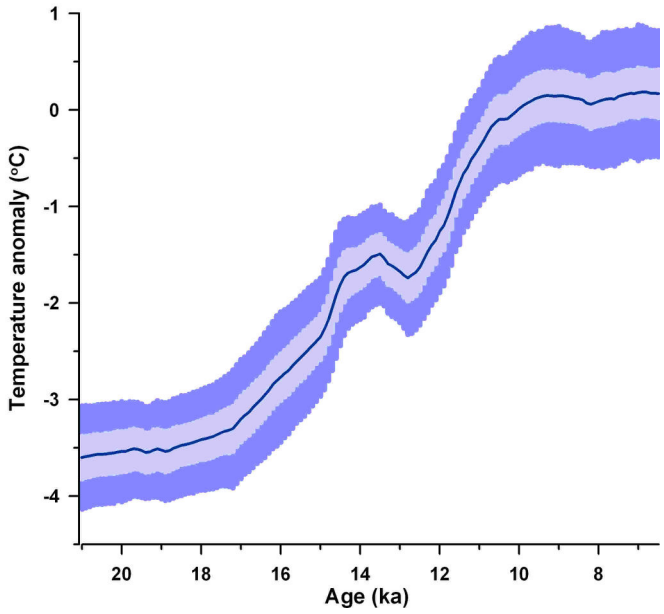

Figure S16: Jackknifed temperature stacks. The unweighted global proxy stack with 1σ error bars derived from 1000 jackknifed stacks randomly excluding 50% (light blue errors) and 90% (dark blue errors) of the records.

5.3 Proxy type

To assess how our temperature reconstructions may be affected by disagreement among the proxies we calculated separate stacks for each proxy type (Figure S17) as well as jackknifed global and hemispheric stacks leaving out one proxy at a time (Figure S18). Differing temperature histories are expected for each proxy type to some extent given the large range in the number and locations of records for each proxy (Figure 1 in the main paper). There is general consistency among the jackknifed global stacks of a two-step deglaciation during the Oldest and Youngest Dryas intervals, with relatively stable temperatures during the Last Glacial Maximum, Bølling/Allerød, and early Holocene. Thus, the correlations between the jackknifed stacks and CO_2 from 22-6.5 ka are all similar ranging from r^2=0.90 to 0.95, as are the temperature lags behind CO_2 based on 20-10 ka lag correlations ranging from 300 to 600 years. The timing of initial warming and the magnitude of the glacial-interglacial change varies among the jackknifed stacks, however. Also, excluding the Mg/Ca records yields a moderate 0.25°C global warming during the early Holocene (Figure S17), which would increase its correlation with ice-sheet retreat and perhaps imply a somewhat larger role for ice-sheet forcing on the temperature stack. We evaluated whether this cooling trend in Mg/Ca is an artifact of an early Holocene peak in carbonate preservation[77] by comparing early Holocene Mg/Ca temperature trends with core depth, since carbonate preservation effects are expected to exert a larger impact on deeper sites. We find little correlation between temperature trend and depth, however, suggesting this early Holocene feature is not an artifact of carbonate preservation (Figure S19).

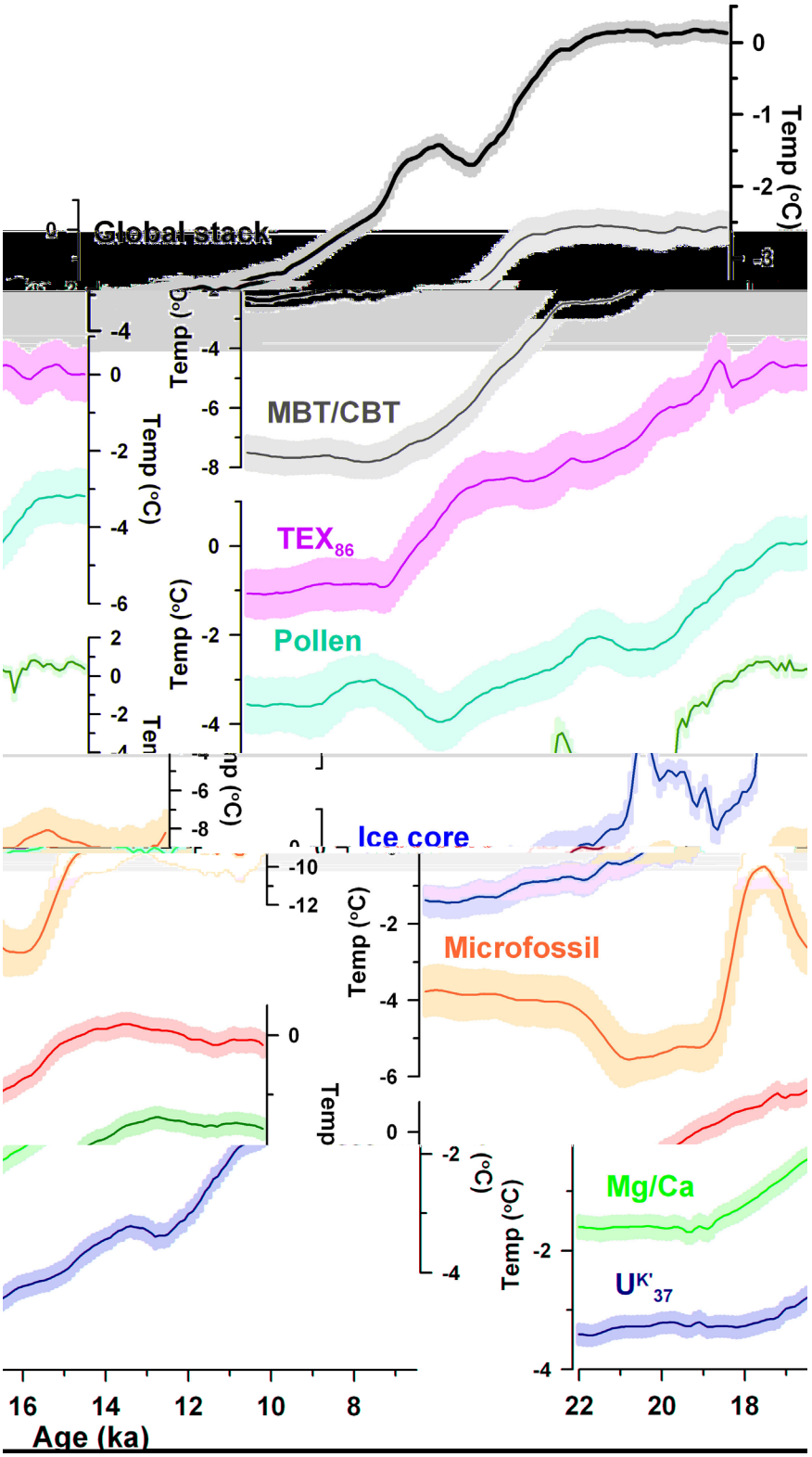

Figure S17: Unweighted temperature stacks by proxy type, with 1σ errors reflecting chronological and temperature calibration uncertainties in the records. The global temperature stack is shown at the top for reference.

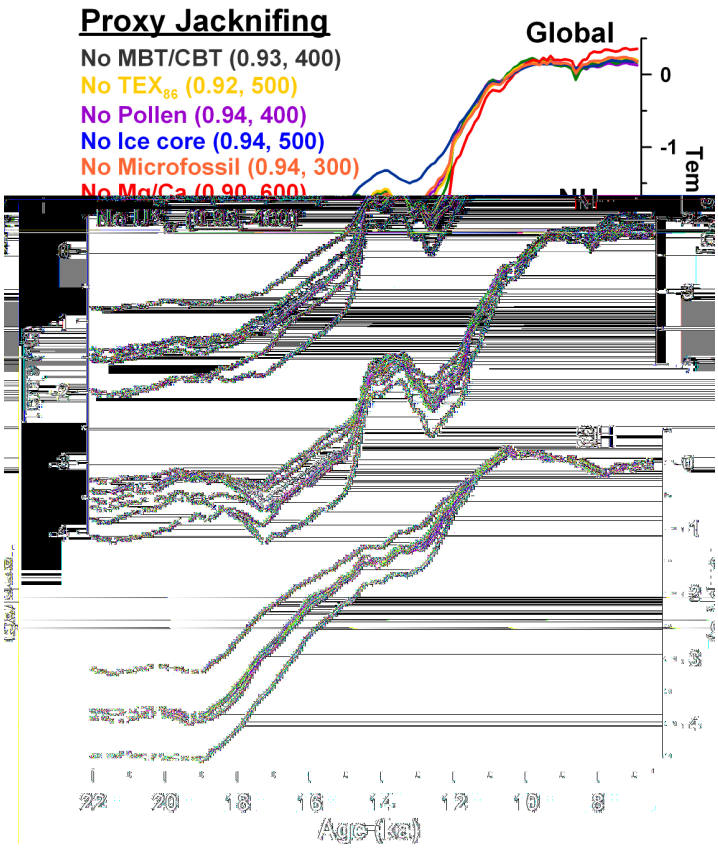

Figure S18: Jackknifing by proxy type. Jackknifed (**top**) global, (**middle**) Northern Hemisphere, and (**bottom**) Southern Hemisphere temperature stacks, leaving one proxy type out at a time. Numbers in parentheses give global stack correlation (r^2) with CO_2 from 22-6.5 ka and lag behind CO_2 (years) determined from lag correlations over 20-10 ka. Note that these stacks are not area-weighted.

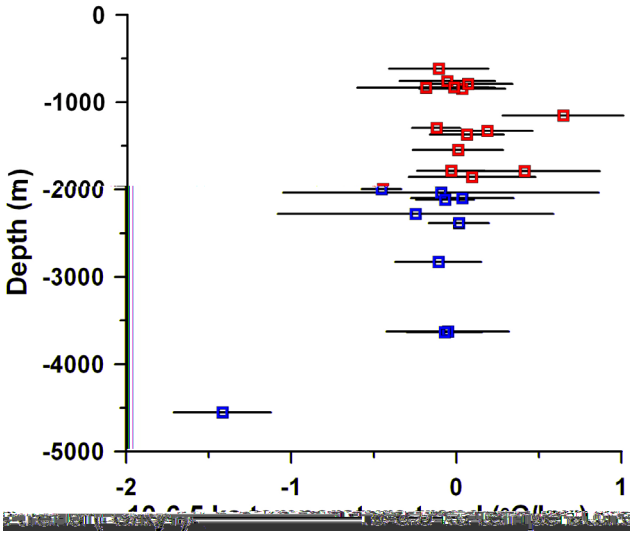

Figure S19: Early Holocene (10-6.5 ka) temperature trends in Mg/Ca records plotted against core depth. Errors (1σ) reflect age-model and temperature calibration uncertainties.

In Figure S20 we plot the 21.5-19 and 19-17.5 ka temperature trends by proxy type to better diagnose the source of the early, pre-CO_2-rise warming. Greenland warming stands out during the earlier interval, with few other records outside of the northern extratropics exhibiting temperature trends significantly different from zero. During the later interval, the interhemispheric seesaw event is evident and seen in multiple proxies. Nonetheless, there are some notable differences among the proxies from 19-17.5 ka. Three TEX_{86} and one MBT/CBT record from 10-35°N warm strongly as compared to Mg/Ca, alkenones, and forams. Also, Mg/Ca records from 30°N-30°S generally show greater warming trends than alkenones, averaging 0.37°C/kyr versus 0.03°C/kyr. Thus, the warming of the northern tropics during this interval, and the resulting net global warming, may be largely attributable to Mg/Ca and TEX_{86}.

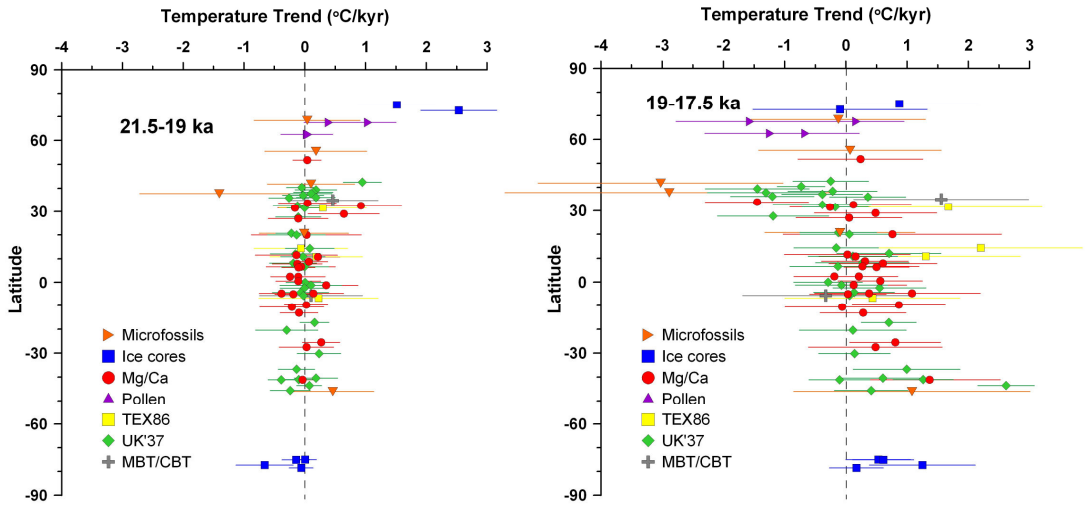

Figure S20: Site-by-site early deglacial temperature trends. Linear temperature trends versus latitude from (**left**) 21.5-19 ka and (**right**) 19-17.5 ka plotted by proxy type. Errors (1σ) reflect age-model and temperature calibration uncertainties.

5.4 Missing data values

There is nearly complete data coverage of the study interval; however, ~15% of the records do not extend entirely through the Last Glacial Maximum and early Holocene

(Figure S1c). To address this issue, we used the Regularized Expectation Maximization (RegEM) method[78] to statistically infill missing values. This adjustment has negligible impact on the temperature stack. We use the infilled data in the main paper.

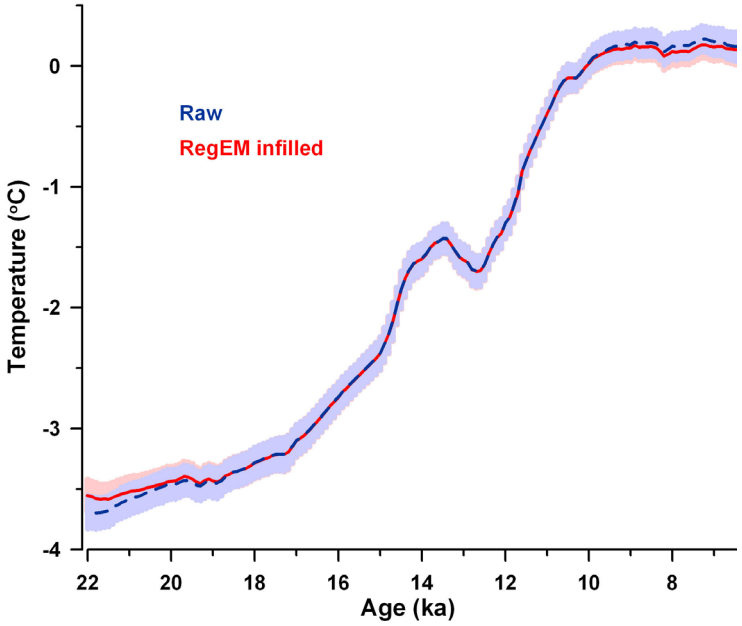

Figure S21: Raw versus infilled temperature data. The temperature stack based on the raw (blue) and statistically-infilled (red) datasets. Errors (1σ) reflect age-model and temperature calibration uncertainties.

5.5 Radiocarbon calibration

67 of the 80 proxy records are anchored solely by radiocarbon dates. We tested the sensitivity of the temperature stack to the choice of radiocarbon calibration by recalibrating all dates with the two most recent calibrations, IntCal04 and IntCal09. While these calibrations are very similar over most of their duration, they differ by up to nearly 1-kyr during the Heinrich-1 interval (Figure S22). Accordingly, the two calibrations yield essentially identical temperature stacks except during Heinrich 1, when they are offset by ~350 years (Figure S23). We reason that the stack is shifted by only 350 years, rather than the full 1-kyr difference between the calibrations, because many of

the proxy records do not have radiocarbon dates in this interval and thus are unaffected. Nonetheless, this offset is important, especially as it occurs during the initial rise in CO_2. For instance, while CO_2 generally leads the temperature stack from 20-10 ka regardless of the calibration, the lead is 460 ± 340 years with IntCal04 but 350 ± 340 years with IntCal09 (Figure S24).

We favor the IntCal04 calibration for the following reasons:

In the IntCal09 paper, Reimer et al.[79] wrote that "the Iberian Margin data generally agree within 2 standard deviations with the Cariaco data and other calibration data. The only notable discrepancy occurs between 15–17.5 cal ka, corresponding to the Heinrich 1 climatic event. This systematic difference could be suppressed by assuming a larger reservoir age for the Iberian Margin. However, such ad hoc corrections may not apply since available data measured on other archives (the few corals in Figure 2 and Bahamas speleothem by Hoffmann et al. [2010]) support the Iberian Margin record. Like the Cariaco record, the present MD952042 [Iberian] chronology must be considered a work in progress awaiting refinement by correlation with more independent data from other archives (corals, speleothems,and marine cores from other oceans)."

Two recent studies have confirmed that the Iberian margin dating is indeed correct. Specifically, climate records developed from deep-sea sediments from the Pakistan Margin can be securely tuned to the Hulu $\delta^{18}O$ record[80] and a new ^{14}C-U/Th dataset generated with coral samples cored offshore Tahiti[81] demonstrate that IntCal04 was more accurate than IntCal09 in the time range corresponding to the early deglaciation, notably the Heinrich 1 event and Oldest Dryas period. The discrepancy can be illustrated by calibrating a ^{14}C age of 13.5 ka BP, which is about 16 cal ka BP with

IntCal04 and 17 cal ka BP with IntCal09 (see Figure S22 that compiles the IntCal09 dataset together with some additional data from the Pakistan Margin).

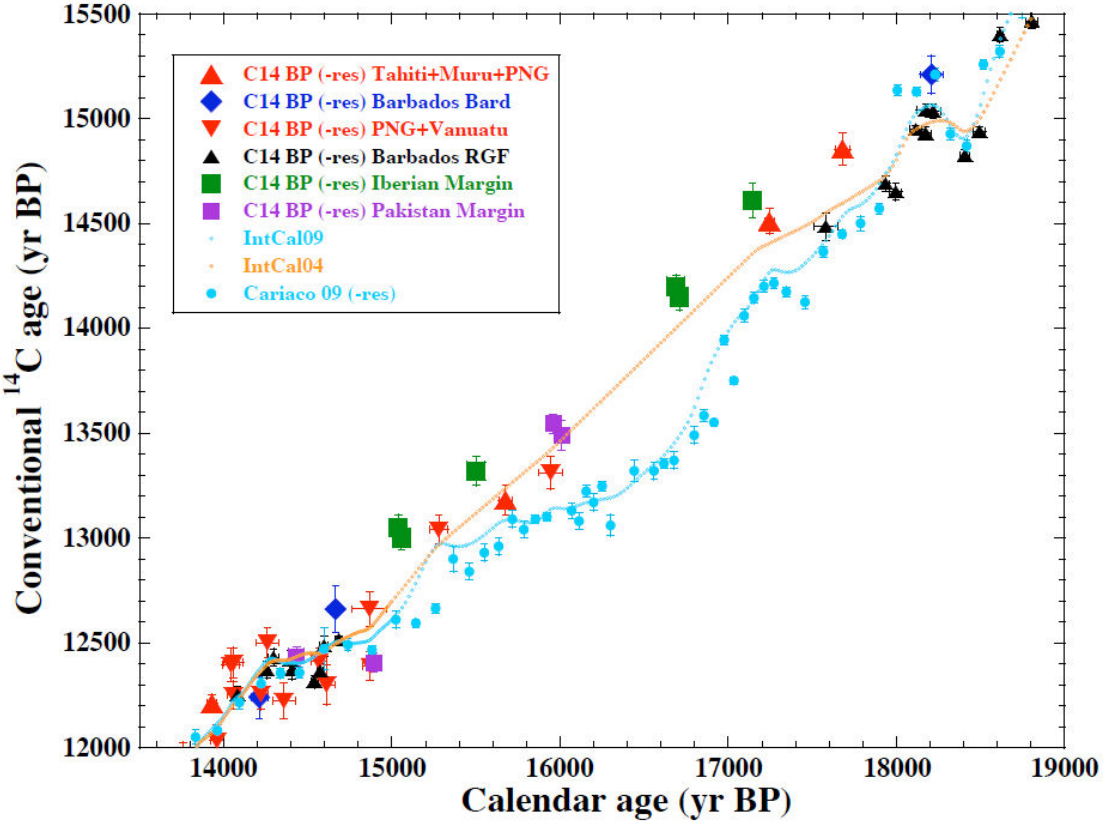

Figure S22: ^{14}C ages plotted versus calendar ages in the interval between 13,500 and 19,000 cal yr BP. Blue diamonds, red and black triangles show the coral data from Barbados, Tahiti, Mururoa, New Guinea and Vanuatu corals. These datasets were used to construct the IntCal09 curve (see Reimer et al.[79] and references therein for the individual records). The light blue dots, green and purple squares show ^{14}C results on planktonic foraminifera from marine sediments tuned to the Hulu speleothem δ^{18}O record independently dated with U-Th ages (the Cariaco Basin and Iberian Margin datasets were also used for constructing the IntCal09 curve, the new Pakistan Margin results are from Bard et al.[80]). All ^{14}C ages are corrected for site-specific reservoir ages (see Reimer et al.[79]) and errors are quoted at the 1σ level. Dotted lines show the resulting calibration curves: in light blue the IntCal09 curve[78] and in orange the previous IntCal04 curve[79] that did not take into account the Cariaco data in this time range (see discussion in Reimer et al.[79]).

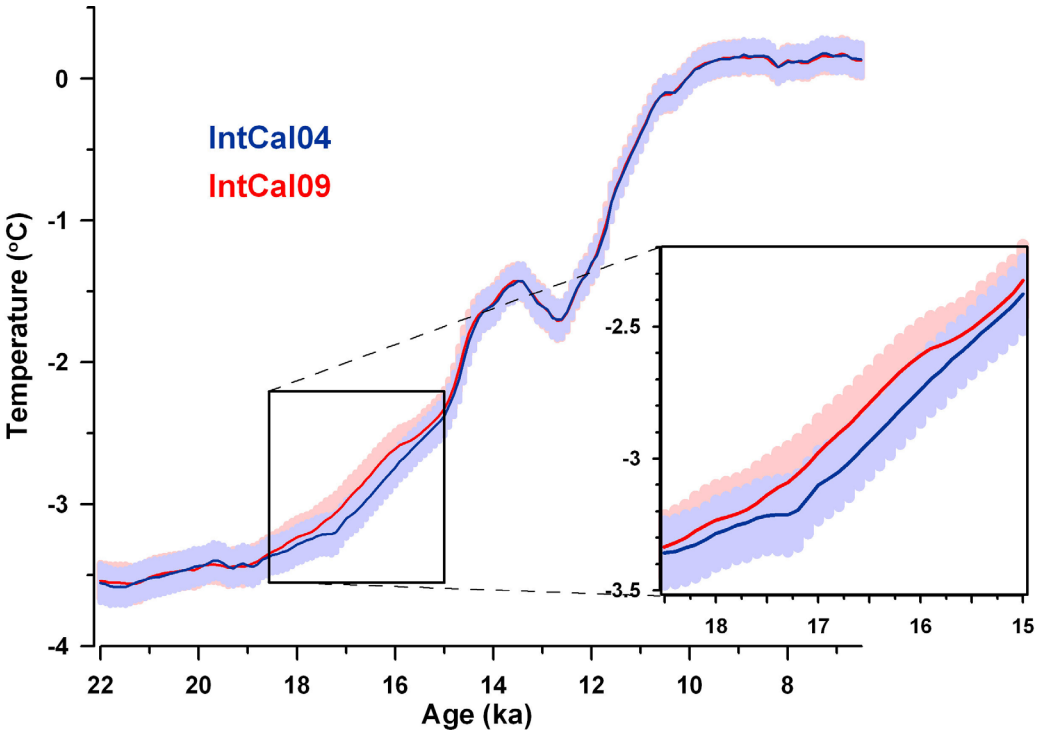

Figure S23: The proxy temperature stack based on the IntCal04 and IntCal09 radiocarbon calibrations. The inset plot shows the interval of disagreement from 18.5-15 ka. Errors (1σ) reflect age-model and temperature calibration uncertainties.

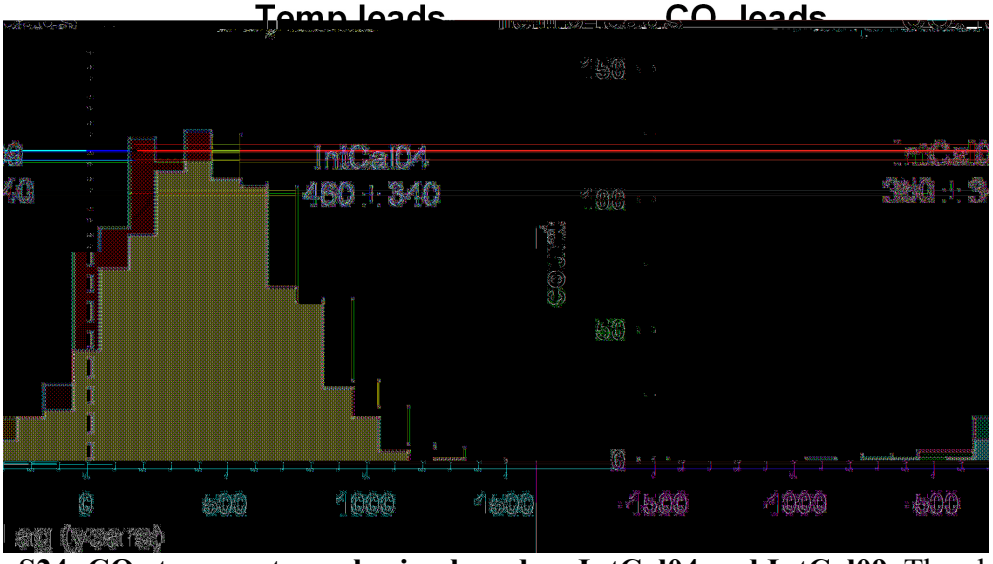

Figure S24: CO_2-temperature phasing based on IntCal04 and IntCal09. The phasing of CO_2 and the global proxy temperature stack based on the IntCal09 (red) and IntCal04 (blue) radiocarbon calibrations using lag correlations from 20-10 ka. The histograms show the result of 1000 realizations, perturbing the proxy records with age model and temperature uncertainties and the CO_2 record with age model errors. The mean and standard deviation of the histograms are given.

6. CO_2-temperature relationship

6.1 Phasing through time

In the main text we discuss the phasing of CO_2 and temperature over the entire 20-10 ka interval. Here, we calculate running phase relationships between CO_2 and the global temperature stack as well as EDC temperature to address how phasing may have varied through time. Phasing is calculated using lag correlations, and we vary time window widths from 3 to 7 kyr. The results indicate Antarctic temperature led CO_2 by a small amount throughout the deglaciation (Figure S25a). The global temperature stack, on the other hand, was synchronous with or lagged CO_2, except at the onset of deglaciation when it led (Figure S25b).

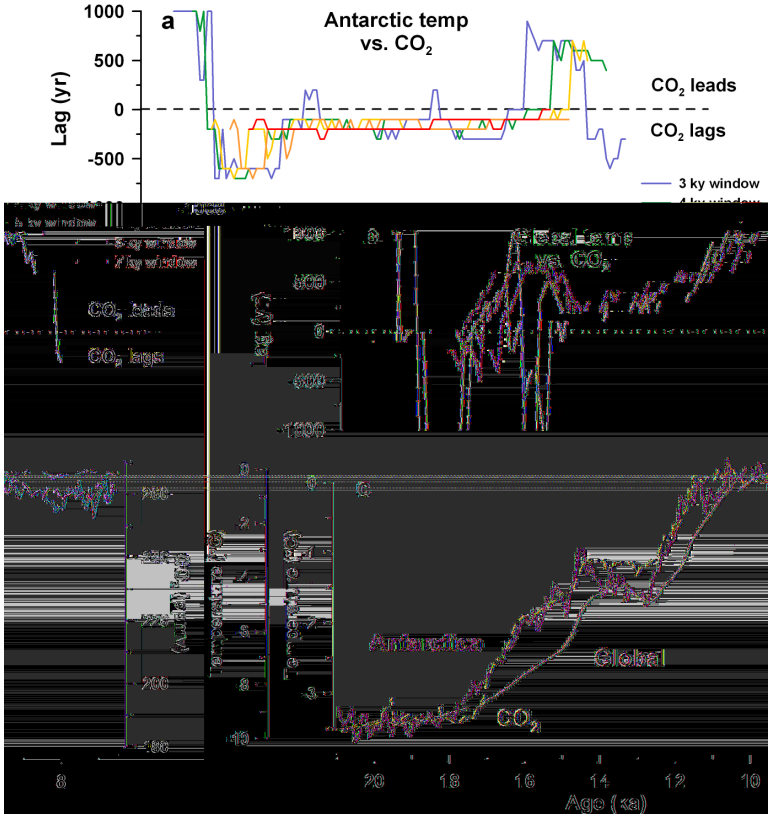

Figure S25: Running temperature-CO_2 lag correlations. (a) Running phasing of CO_2 and EPICA Dome C over the last deglaciation, both on the timescale from ref. 64. The different colors indicate the window width used to compute lag correlations. **(b)** Same as (a), but for CO_2 and the global temperature stack. **(c)** The time series used in (a) and (b).

6.2 Breakfit

While we focus on lag correlations to determine phasing in the main text, here we include an alternative evaluation of this issue. The function Breakfit[82] provides an objective identification of transition points in time series, which allows us to assess the relative timing of changes in the CO_2 and global temperature records. We determine the timing of four transition points in the records and apply the same search windows to both time series for consistency. The same seed generator number (200) is used in each case, 200 bootstrap iterations are used to quantify errors, and standard deviations of 0.15°C and 3 ppmv are used for temperature and CO_2. The results indicate that CO_2 was either synchronous within error or led temperature at the starts of the deglaciation, Bølling, and Younger Dryas, and Holocene (Figure S26; Table S2).

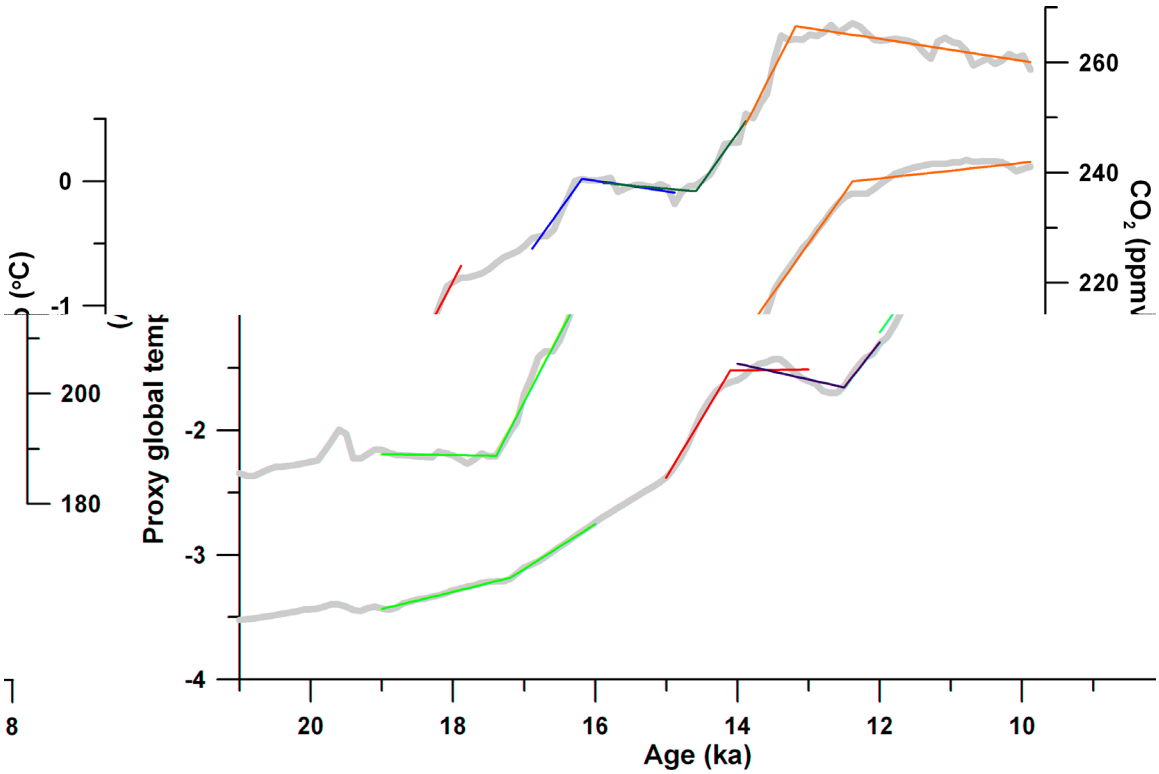

Figure S26: Objectively defined change-points. Breakfit[82] functions (colored lines) applied to the CO_2 (top) and global temperature stack (bottom).

Table S2: Breakfit[82] identification of deglacial transition points. Errors are 1σ.

		CO_2	Temperature
Event	Search window	Age (ka)	Age (ka)
Deglacial onset	19-16 ka	17.40 ± 0.03	17.20 ± 0.03
Bølling	15-13 ka	14.29 ± 0.06	14.10 ± 0.06
Younger Dryas	14-12 ka	12.70 ± 0.06	12.50 ± 0.08
Holocene	12-8 ka	11.29 ± 0.05	10.8 ± 0.04

6.3 Detrending

Tests with synthetic time series suggest that detrending records with ramp structures can increase the resolving power of lag correlations to determine lead-lag relationships (Figure S27). Lag correlations between CO_2 and the global temperature stack from 20-10 ka after detrending yield similar results to those for the undetrended time series presented in Figure 1b in the main paper (Figure S28).

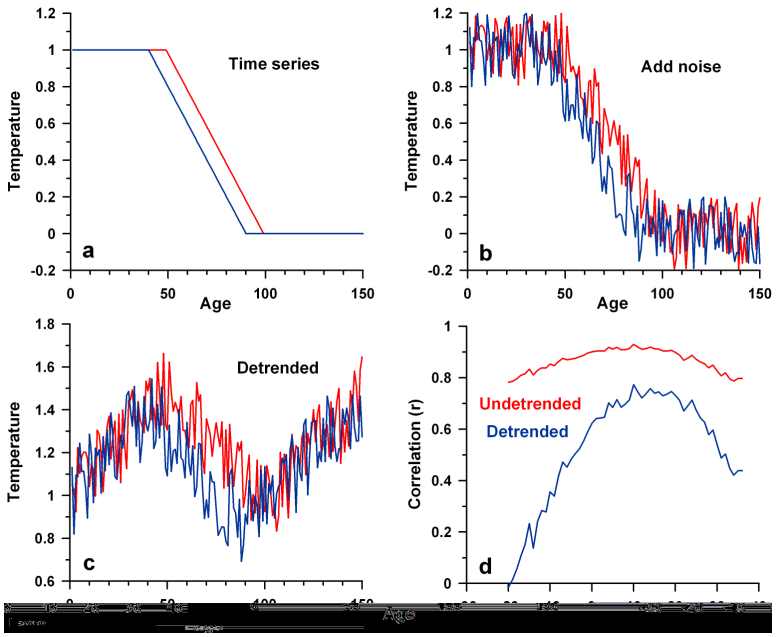

Figure S27: Synthetic time series showing how detrending increases the resolving power of lag correlations. (**a**) Ramped time series with a 10 unit phase offset. (**b**) With noise added. (**c**) Linearly detrended. (**d**) Lag correlations between the detrended (blue) and undetrended (red) noisy time series.

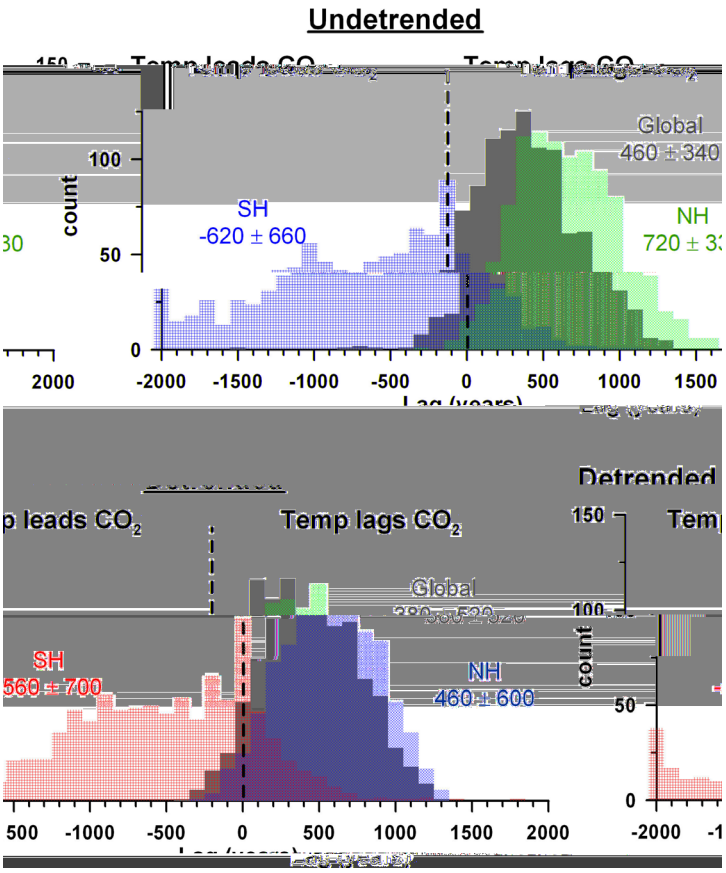

Figure S28: CO_2-temperature phasing using raw and detrended time series. Histograms showing the lead-lag relationship based on lag correlations from 20-10 ka between CO_2 and the proxy global (gray), Northern Hemisphere (blue), and Southern Hemisphere (red) temperature stacks before (top) and after (bottom) detrending. The histograms show the results of 1000 realizations after perturbing the temperature records with age model and proxy temperature errors and the CO_2 record with age model errors. The mean and standard deviation of each histogram are given.

6.4 CO_2 versus CO_2+CH_4+N_20

While we focus on CO_2 in the manuscript since it dominated the deglacial greenhouse gas forcing (Figure S29), CH_4 and N_2O are also globally well-mixed greenhouse gases and would be expected to affect global temperature. The correlations of the global temperature stack with CO_2 forcing and combined CO_2+CH_4+N_2O forcing are similar (r^2=0.94 and 0.93), as are the temperature lags behind each (460±340 yr and

250±340) (Figure S29), supporting our conclusion that greenhouse gases were an important driver of deglacial warming.

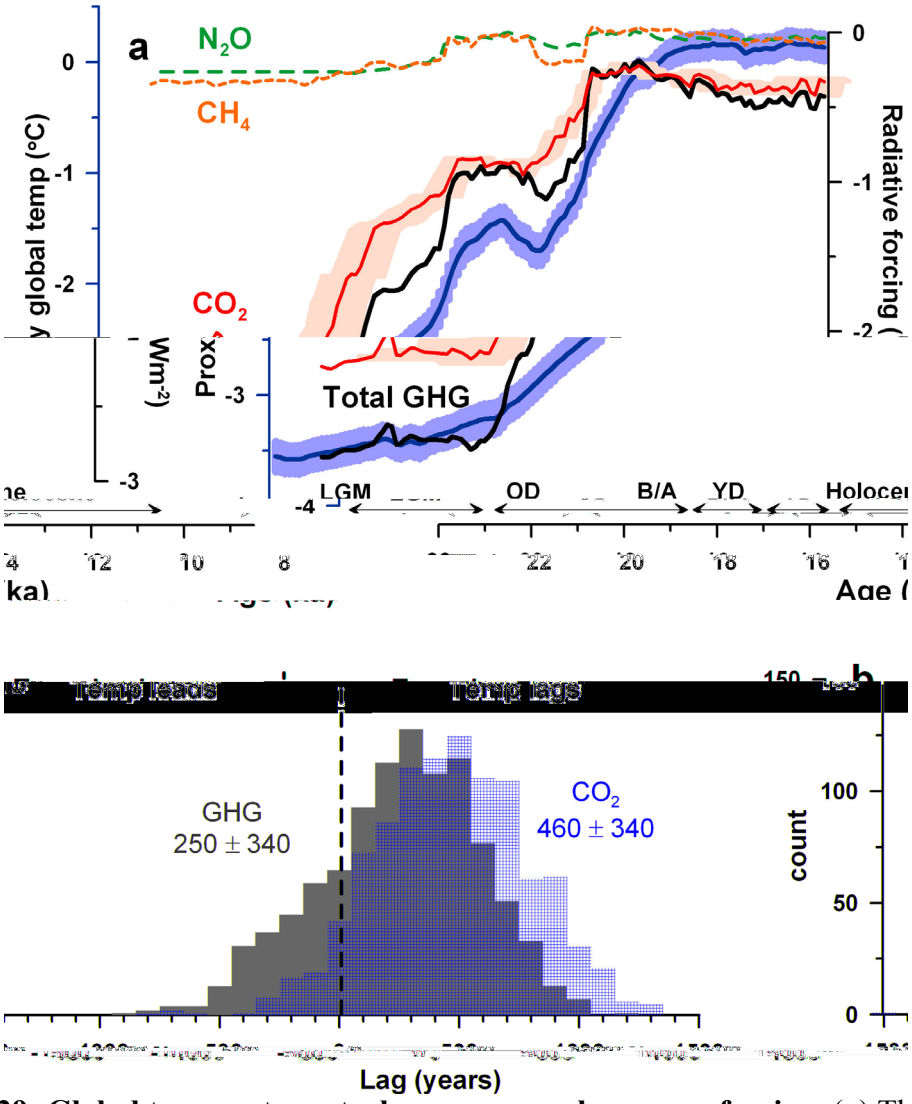

Figure S29: Global temperature stack versus greenhouse-gas forcing. (**a**) The global temperature stack (blue), and the radiative forcing from N_2O (dashed green), CH_4 (dotted orange), and CO_2 (solid red), as well as their combined forcing (thick black) using the simplified expressions from ref. 83. CO_2 age-model uncertainty (1σ) is shown (see section 2.3). (**b**) The phasing of the global temperature stack with CO_2 (red) and combined greenhouse gas-forcing (gray) based on lag correlations from 20-10 ka. 1000 realizations are shown, perturbing the proxy records with age model and temperature errors, and the CO_2 and combined greenhouse gas-forcing curves with CO_2 age model errors (see Section 2.3). The mean and standard deviation of the histograms are given.

7. Model freshwater forcing

As emphasized in the paper, several model freshwater forcing scenarios were tested, and the scenario that produced North Atlantic climate variability in closest agreement with proxy records was used for the final simulation (Figure S30).

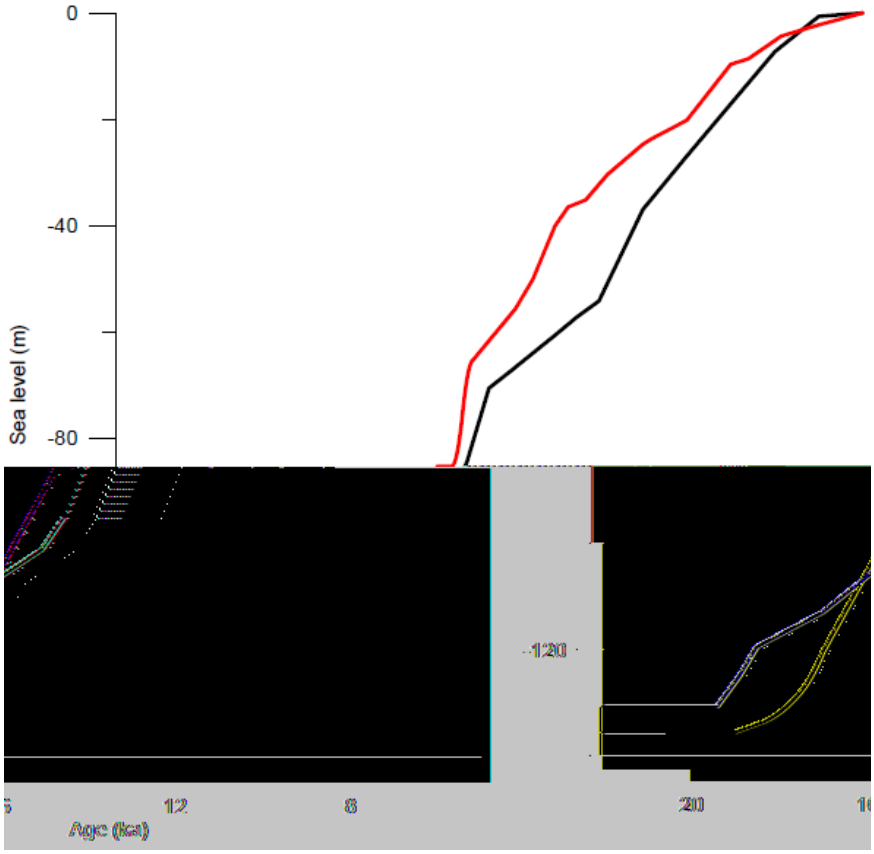

Figure S30: The freshwater flux added to the model shown as equivalent sea level (red) and reconstructed eustatic sea level[84] (black).

8. Comparison with Schmittner et al. (2011)[85]

The glacial-interglacial warming in our proxy temperature stack is ~3.6°C, which is larger than a recent estimate of 2.6°C by Schmittner et al.[85]. We examine here the reasons for this difference. Fundamentally, the data used in this study are a small subset of the much larger LGM dataset used by Schmittner et al., which also included the MARGO[86] sea-surface and Bartlein et al.[87] continental temperature reconstructions (80 individual reconstructions in this study versus 1,100 in Schmittner et al.). As the Schmittner et al. results are strongly influenced by MARGO, we compared the consistency of our dataset with MARGO at the 35 5° x 5° grid cells where both have data, which range from 57.5°N to 47.5°S. Of these 35 grid cells, 22 have completely independent data (i.e., our proxy records at these locations are not included in MARGO) while 13 have redundant data (i.e., our proxy records at these locations are included in MARGO, in addition to others). The area-weighted mean LGM cooling at the 22 cells containing entirely independent data is -3.1°C for MARGO and -2.9°C for our dataset (n=9 Mg/Ca, n=15 alkenones, n=3 foram assemblages n=3 TEX_{86}), and -3.2°C for both MARGO and our dataset (n=4 Mg/Ca, n=8 alkenones, n=1 foram assemblage) at the 13 cells containing redundant data (Table S3). Since MARGO has a global SST cooling of -1.9±1.8°C, the larger cooling at our grid cells suggests that our ocean data are biased toward more sensitive sites. In summary, where we have common ocean data coverage, our results are in close agreement with the Schmittner et al. dataset (i.e., MARGO), but the greater spatial data coverage in Schmittner et al. versus this study and Shakun and Carlson[88] indicates that the Schmittner et al. data are more representative of the LGM to modern temperature difference.

Table S3: Last Glacial Maximum temperature anomalies

	Model	**Proxy data**		
	Schmittner et al.[85]	This study	MARGO[86]	Bartlein et al.[87]
SST ocean	-1.7±0.4°C *	-3.2°C (n=53) ^	-1.9±1.8°C (n=307)	-
SAT land	-4.6±0.7°C **	-6.4°C (n=14) ^	-	-6.1°C (n=98)
SST shared ocean grid cells (independent data)	-	-2.9°C (n=22) ^^	-3.1°C (n=22)	-
SST shared ocean grid cells (redundant data)	-	-3.2°C (n=13) ^^	-3.2°C (n=13)	-
SAT global land+ SST global ocean	-2.6±0.5°C ***	-	-	-
SAT global land+ SAT global ocean	-3.3±0.5°C ****	-	-	-

"SAT" = surface air temperature. "SST" = sea surface temperature. "n" is number of grid cells; Schmittner et al., this study, and MARGO are based on a 5° x 5° grid, while Bartlein et al. is on a 2° x 2° grid.

* global model mean (interpolated to median of PDF) 66% interval = [-1.3;-2.0]

** global model mean (interpolated to median of PDF) 66% interval = [-3.9:-5.2]

*** global model mean (interpolated to median of PDF) 66% interval = [-2.0:-2.9]

**** global model mean (interpolated to median of PDF) 66% interval = [-2.4:-3.5]

^ LGM (19-23 ka) anomalies from early Holocene (6.5-10.5 ka) mean

^^ LGM (19-23 ka) anomalies from late Holocene (2-0 ka) mean for proxy records that extend to present or WOA98 (ref. 89) 10-m depth temperatures for records that end before 2 ka.

References

1. Cuffey, K. M. & Clow, G.D. Temperature, accumulation, and ice sheet elevation in central Greenland through the last deglacial transition. *J. of Geophy. Res.* **102**, 26383-26396 (1997).
2. Andersen, K. K. *et al.* The Greenland Ice Core Chronology 2005, 15-42 ka. Part 1: Constructing the time scale. *Quat. Sci. Rev.* **25**, 3246-3257, doi:10.1016/j.quascirev.2006.08.002 (2006).
3. Rasmussen, S. O. *et al.* A new Greenland ice core chronology for the last glacial termination. *J. Geophys. Res.* **111**, doi:10.1029/2005JD006079 (2006).
4. Rasmussen, S. O. *et al.* Synchronization of the NGRIP, GRIP, and GISP2 ice cores across MIS 2 and palaeoclimatic implications. *Quat. Sci. Rev.* **27**, 18-28, doi:10.1016/j.quascirev.2007.01.016 (2008).
5. Kurek, J., Cwynar, L. C., Ager, T. A., Abbott, M. B. & Edwards, M. E. Late Quaternary paleoclimate of western Alaska inferred from fossil chironomids and its relation to vegetation histories. *Quat. Sci. Rev.* **28**, 799-811 (2009).
6. Viau, A.E., Gajewski, K., Sawada, M. C. & Bunbury, J. Low-and high frequency climate variability in Eastern Beringia during the past 25,000 years. *Canadian J. Earth Sci.* **45**, 1435-1453 (2008).
7. Waelbroeck, C. *et al.* The timing of the last deglaciation in North Atlantic climate records. *Nature* **412**, 724-727 (2001).
8. Peck, V. L., Hall, I. R., Zahn, R. & Elderfield, H. Millennial-scale surface and subsurface paleothermometry from the northeast Atlantic, 55-8 ka BP. *Paleoceanography* **23**, doi:10.1029/2008PA001631 (2008).
9. Prahl, F.G., Pisias, N. G., Sparrow, M. A. & Sabin, A. Assessment of sea-surface temperature at 42 degrees north in the California current over the last 30,000 years. *Paleoceanography* **10**, 763-773 (1995).
10. Minoshima, K, Kawahata, H. & Ikehara, K. Changes in biological production in the mixed water region of the northwestern North Pacific during the last 27 kyr. *Palaeogeog. Palaeoclim. Palaleoecol.* **254**, 430-447 (2007).
11. Cacho, I., Grimalt, J. O., Canals, M., Sbaffi, L. & Shackelton, N. J. Variability of the western Mediterranean Sea surface temperature during the last 25,000 years and its connection with the Northern Hemisphere climatic changes. *Paleoceanography* **16,** 40-52 (2001).
12. Bard, E., Rostek, F., Turon, J.-L. & Gendreau, S. Hydrological impact of Heinrich events in the subtropical northeast Atlantic. *Science* **289,** 1321-1324 (2000).
13. Calvo, E. Villanueva, J., Grimalt, J. O., Boelaert, A. & Labeyrie, L. New insights into the glacial latitudinal temperature gradients in the North Atlantic. Results from $U^{K'}_{37}$ sea surface temperatures and terrigenous inputs. *Earth Planet Sci. Lett.* **188**, 509–519 (2001).
14. Cacho, I. *et al.* Dansgaard-Oeschger and Heinrich Event imprints in Alboran Sea paleotemperatures. *Paleoceanography* **14,** 698-705 (1999).
15. Isono, D. *et al.* The 1500-year climate oscillation in the midlatitude North Pacific during the Holocene. *Geology* **37**, 591-594 (2009).
16. Peterse, F. *et al.* Decoupled warming and monsoon precipitation in East Asia over the last deglaciation. *Earth Plan. Sci. Lett.* **301**, 256-264 (2011).

17. Carlson, A. E. *et al.* Subtropical salinity variability and Atlantic meridional circulation during deglaciation. *Geology* **12**, 991-994 (2008).
18. Sawada, K. & Handa, N. Variability of the path of the Kuroshio ocean current over the past 25,000 years. *Nature* **392**, 592-595 (1998).
19. Castañeda, I.S. *et al.* Millennial-scale surface temperature changes in the eastern Mediterranean (Nile River Delta region) over the last 27,000 years. *Paleoceanography* **25**, PA1208, doi:10.1029/2009PA001740 (2010).
20. Kubota, Y. *et al.* Variations of East Asian summer monsoon since the last deglaciation based on Mg/Ca and oxygen isotope of planktonic foraminifera in the northern East China Sea. *Paleoceanography* **25**, PA4205, doi:10.1029/2009PA001891 (2010).
21. Ijiri, A. *et al.* Paleoenvironmental changes in the northern area of the East China Sea during the past 42,000 years. *Palaeogeog. Palaeoclim. Palaleoecol.* **219**, 239-261 (2005).
22. Ziegler, M., Nürnberg, D., Karas, C., Tiedemann, R. & Lourens, L. J. Persistent summer expansion of the Atlantic Warm Pool during glacial abrupt cold events. *Nature Geo.* **1**, 601-605 (2008).
23. Arz, H. W., Pätzold, J., Müller, P. J. & Moammar, M. O. Influence of Northern Hemisphere climate and global sea level rise on the restricted Red Sea marine environment during termination I, *Paleoceanography* **18**, 1053, doi:10.1029/2002PA000864 (2003).
24. Flower, B. P., Hastings, D. W., Hill, H. W. & Quinn, T. M. Phasing of deglacial warming and Laurentide Ice Sheet meltwater in the Gulf of Mexico. *Geology* **32,** 597-600 (2004).
25. deMenocal, P. B., Ortiz, J., Guilderson, T. & Sarnthein, M. Coherent high- and low-latitude climate variability during the Holocene warm period. *Science* **288,** 2198-2202 (2000).
26. Zhao, M., Beveridge, N., Shackleton, N., Sarnthein, M. & Eglington, G. Molecular stratigraphy of cores off northwest Africa: Sea surface temperature history over the last 80ka. *Paleoceanography* **10,** 661-675 (1995).
27. Pelejero, C., Grimalt, J. O., Heilig, S., Kienast, M. & Wang, L. High-resolution U^{k}_{37} temperature reconstructions in the South China Sea over th past 220 kyr. *Paleoceanography* **14,** 224-231 (1999).
28. Wei, G., Deng, W., Liu, Y. & Li, X. High-resolution sea surface temperature records derived from foraminiferal Mg/Ca ratios during the last 260 ka in the northern South China Sea. *Palaeogeog. Palaeoclim. Palaleoecol.* **250**, 126-138 (2007).
29. Huguet, C., J.-H. Kim, J. S. S. Damste´ & S. Schouten. Reconstruction of sea surface temperature variations in the Arabian Sea over the last 23 kyr using organic proxies (TEX_{86} and $U^{K'}_{37}$). *Paleoceanography* **21**, PA3003, doi:10.1029/2005PA001215 (2006).
30. Rühlemann, C., Mulitza, S., Muller, P. J., Wefer, G. & Zahn, R. Warming of the tropical Atlantic Ocean and slowdown of thermohaline circulation during the last deglaciation. *Nature* **402,** 511-514 (1999).

31. Schmidt, M. W., Spero, H. J. & Lea, D. W. Links between salinity variation in the Caribbean and North Atlantic thermohaline circulation. *Nature* **428,** 160-163 (2004).
32. Lea, D. W., Pak, D. K., Peterson, L. C. & Hughen, K. A. Synchroneity of tropical and high-latitude Atlantic temperatures over the last glacial termination. *Science* **301,** 1361-1364 (2003).
33. Rosenthal, Y., Oppo, D. & Linsley, B. K. The amplitude and phasing of climate change during the last deglaciation in the Sulu Sea, western equatorial Pacific. *Geophys. Res. Lett.* **30,** doi:10.1029/2002GL016612 (2003).
34. Leduc, G. *et al.* Moisture transport across Central America as a positive feedback on abrupt climatic changes. *Nature* **445**, 908-911 (2007).
35. Benway, H. M., Mix, A. C., Haley, B. A. & Klinkhammer, G. P. Eastern Pacific warm pool paleosalinity and climate variability: 0-30 kyr. *Paleoceanography* **21,** doi:10.1029/2005PA001208 (2006).
36. Steinke, S. *et al.* Proxy dependence of the temporal pattern of deglacial warming in the tropical South China Sea: toward resolving seasonality. *Quat. Sci. Rev.* **27**, 688-700 (2008).
37. Stott, L., Timmermann, A. & Thunell, R. Southern hemisphere and deep-sea warming led deglacial atmospheric CO_2 rise and tropical warming. *Science* **318,** 435-438 (2007).
38. Weldeab, S., Lea, D. W., Schneider, R. R. & Andersen, N. 155,000 years of West African Monsoon and ocean thermal evolution. *Science* **316,** 1303-1307 (2007).
39. Weldeab, S., Schneider, R. R., Kölling, M. & Wefer, G. Holocene African droughts relate to eastern equatorial Atlantic cooling. *Geology* **33,** 981-984 (2005).
40. Lea, D. W. *et al.* Paleoclimate history of Galápagos surface waters over the last 135,000 yr. *Quat. Sci. Rev.* **25,** 1152-1167 (2006).
41. Kienast, M. *et al.* Eastern Pacific cooling and Atlantic overturning circulation during the last deglaciation. *Nature* **443,** 846-849 (2006).
42. Koutavas, A. & Sachs, J. P. Northern timing of deglaciation in the eastern equatorial Pacific from alkenone paleothermometry. *Paleoceanography* **23**, PA4205, doi:10.1029/2008PA001593 (2008).
43. Koutavas, A., Lynch-Stieglitz, J., Marchitto, T. M., Jr. & Sachs, J. M. El Niño-like pattern in Ice Age tropical Pacific sea surface temperature. *Science* **297,** 226-230 (2002).
44. Jaeschke, A., Rühlemann, C., Arz, H. W., Heil, G. & Lohmann, G. Coupling of millennial-scale changes in sea surface temperature and precipitation off northeastern Brazil with high-latitude climate shifts during the last glacial period. *Paleoceanography* **22**, PA4206, doi:10.1029/2006PA001391 (2007).
45. Weldeab, S., Schneider, R. R. & Kölling, M. Deglacial sea surface temperature and salinity increase in the western tropical Atlantic in synchrony with high latitude climate instabilities. *Earth Planet Sci. Lett.* **241,** 699-706 (2006).
46. Visser, K., Thunell, R. & Stott, L. Magnitude and timing of temperature change in the Indo-Pacific warm pool during deglaciation. *Nature* **421,** 152-155 (2003).

47. Weijers, J. W. H., Schefuß, E., Schouten, S. & Damste, J. S. S. Coupled thermal and hydrological evolution of tropical Africa over the last deglaciation. *Science* **315,** 1701-1704 (2007).
48. Schefuß, E., Schouten, S. & Schneider, R. R. Climatic controls on central African hydrology during the past 20,000 years. *Nature* **437,** 1003-1006 (2005).
49. Tierney, J. E. *et al.* Northern Hemisphere controls on tropical southeast African climate during the past 60,000 years. *Science* **322,** 252-255 (2008).
50. Levi, C. *et al.* Low-latitude hydrological cycle and rapid climate changes during the last deglaciation. *Geochem. Geophys. Geosys.* **8,** doi:10.1029/2006GC001514 (2007).
51. Xu, J., Holbourn, A., Kuhnt, W., Jian, Z. & Kawamura, H. Changes in the thermocline structure of the Indonesian outflow during Terminations 1 and 2. *Earth Planet Sci. Lett.* **273**, 152-162 (2008).
52. Kim, J.-H., Schneider, R. R., Muller, P. J. & Wefer, G. Interhemispheric comparison of deglacial sea-surface temperature patterns in Atlantic eastern boundary currents. *Earth Planet Sci. Lett.* **194,** 383-393 (2002).
53. Bard, E., Rostek, F. & Sonzogni, C. Interhemispheric synchrony of the last deglaciation inferred from alkenone palaeothermometry. *Nature* **385,** 707-710 (1997).
54. Farmer, E. C., DeMendocal, P. B. & Marchitto, T. M. Holocene and deglacial ocean temperature variability in the Benguela upwelling region: Implications for low-latitude atmospheric circulation. *Paleoceanography* **20,** doi:10.1029/2004PA001049 (2005).
55. Kaiser, J., Lamy, F. & Hebbeln, D. A 70-kyr sea surface temperature record off southern Chile (Ocean Drilling Program Site 1233). *Paleoceanography* **20,** doi:10.1029/2005PA001146 (2005).
56. Calvo, E., Pelejero, C., DeDeckker, P. & Logan, G. A. Antarctic deglacial pattern in a 30 kyr record of sea surface temperature offshore South Australia. *Geophys. Res. Lett.* **34**, L13707, doi:10.1029/2007GL029937 (2007).
57. Pahnke, K. & Sachs, J. M. Sea surface temperatures of southern midlatitudes 0–160 kyr B.P. *Paleoceanography* **21,** doi:10.1029/2005PA001191 (2006).
58. Lamy, F. *et al.* Modulation of the bipolar seesaw in the Southeast Pacific during Termination 1. *Earth Planet Sci. Lett.* **259,** 400-413 (2007).
59. Sachs, J. P., Anderson, R. F. & Lehman, S. J. Glacial surface temperatures of the southeast Atlantic Ocean. *Science* **293,** 2077-2079 (2001).
60. Barker, S. *et al.* Interhemispheric Atlantic seesaw response during the last deglaciation. *Nature* **457**, 1097-1102 (2009).
61. Barrows, T. T., Lehman, S. J., Fifield, L. K. & De Deckker, P. Absence of cooling in New Zealand and the adjacent Ocean during the Younger Dryas chronozone. *Science* **318,** 86-89 (2007).
62. Labeyrie, L. *et al.* Hydrographic changes of the Southern Ocean (southeast Indian sector) over the last 230 kyr. *Paleoceanography* **11**, 57-76 (1996).
63. Stenni, B. *et al.* The deuterium excess records of EPICA Dome C and Dronning Maud Land ice cores (East Antarctica). *Quat. Sci. Rev.* **29**, 146-159 (2010).
64. Lemieux-Dudon, B. *et al.* Consistent dating for Antarctic and Greenland ice cores. *Quat. Sci. Rev.* **29**, 8-20 (2010).

65. Kawamura, K. *et al.* Northern Hemisphere forcing of climatic cycles in Antarctica over the past 360,000 years. *Nature* **448,** 912-916 (2007).
66. Petit, J. R *et al.* Climate and atmospheric history of the past 420,000 years from the Vostok ice core, Antarctic. *Nature* **399,** 429-436 (1999).
67. Clark, P. U. *et al.* Global climate evolution during the last deglaciation. *Proc. Natl. Acad. Sci.*, doi:10.1073/pnas.1116619109.
68. Huybers, P & Wunsch, C. A depth-derived Pleistocene age model: Uncertainty estimates, sedimentation variability, and nonlinear climate change. *Paleoceanography* **19**, doi:10.1029/2002PA000857 (2004).
69. Svensson, A. *et al.* A 60 000 year Greenland stratigraphic ice core chronology. *Climate of the Past* **4**, 47-57 (2008).
70. Andersen, K. K. *et al.* The Greenland Ice Core Chronology 2005, 15-42 ka. Part 1: constructing the time scale. *Quat. Sci. Rev.* **25**, 3246-3257 (2006).
71. Pedro, J. B. *et al.* The last deglaciation: timing the bipolar seesaw. *Climate of the Past Discussion* **7**, 397-430 (2011).
72. Blunier, T. *et al.* Synchronization of ice core records via atmospheric gases. *Clim. Past* **3**, 325-330 (2007).
73. Severinghaus, J. P. & Brook, E. J. Abrupt climate change at the end of the last glacial period inferred from trapped air in polar ice. *Science* **286**, 930-934 (1999).
74. Marcott, S. A., Shakun, J. D., Clark, P. U., & Mix, A. C. A reconstruction of Holocene global temperature. *In prep.*
75. Smith, T. M. *et al.* Improvements to NOAA's historical merged land-ocean surface temperature analysis (1880-2006). *J. Clim.* **21**, 2283-2293 (2008).
76. Rayner, N. A. *et al.* Global analyses of sea surface temperature, sea ice, and night marine air temperature since the late nineteenth century. *J. Geophys. Res.* **108**, 4407, doi:10.1029/2002JD002670 (2003).
77. Berger, W. H. Deep-sea carbonate and the deglaciation spike in pteropods and foraminifera. *Nature* **269**, 301-304 (1977).
78. Schneider, T. Analysis of incomplete climate data: Estimation of mean values and covariance matrices and imputation of missing values. *J. Clim.* **14**, 853-871 (2001).
79. Reimer, P. J. *et al.* IntCal09 and Marine09 radiocarbon age calibration curves, 0-50,000 years cal BP. *Radiocarbon* **51**, 1111-1150 (2009).
80. Bard, E., Ménot G. & Licari L. Radiocarbon calibration-comparison records based on marine sediments from the Pakistan and Iberian Margins. *Geophys. Res. Abst.* **11**, EGU2009-6985 (2009).
81. Durand, N *et al.* New insights into the radiocarbon calibration based on 14C and U-Th dating of corals drilled offshore Tahiti (IODP Expedition #310). *Geophys. Res. Abst.* **12**, EGU2010-12689-1 (2010).
82. Mudelsee, M. Break function regression: A tool for quantifying trend changes in climate time series. *Euro. Phys. J. Spec. Top.* **174**, 49-63 (2009).
83. Ramaswamy, V. et al. Radiative forcing of climate change. Climate Change 2001: The Scientific Basis. Contribution of Working Group I to the Third Assessment Report of the Intergovernmental Panel on Climate Change (eds. Houghton, J. T. et al.) (Cambridge Univ. Press, Cambridge, UK, 2001).
84. Clark, P. U. *et al.* The Last Glacial Maximum. *Science* **325**, 710-714 (2009).

85. Schmittner, A. *et al.* Climate sensitivity estimated from temperature reconstructions of the Last Glacial Maximum. *Science* **334**, 1385-1388, doi:10.1126/science.1203513 (2011).
86. MARGO Project Members. Constraints on the magnitude and patterns of ocean cooling at the Last Glacial Maximum. *Nature Geosci.* **2**, 127-132 (2009).
87. Bartlein, P. J. *et al.* Pollen-based continental climate reconstructions at 6 and 21 ka: a global synthesis. *Clim. Dyn.* **37**, doi:10.1007/s00382-010-0904-1.
88. Shakun, J. D. & Carlson, A. E. A global perspective on Last Glacial Maximum to Holocene climate change. *Quat. Sci. Rev.* **29**, 1801-1816 (2010).
89. World Ocean Atlas 1998: <http://ingrid.ldeo.columbia.edu/SOURCES/.NOAA/.NODC/.WOA98/> (NODC, Silver Springs, 1998).

Appendix S1: Age models (blue) with 2σ uncertainties (red lines) for all records based on radiocarbon dating, using the IntCal04 calibration. Radiocarbon dates are shown as black dots.

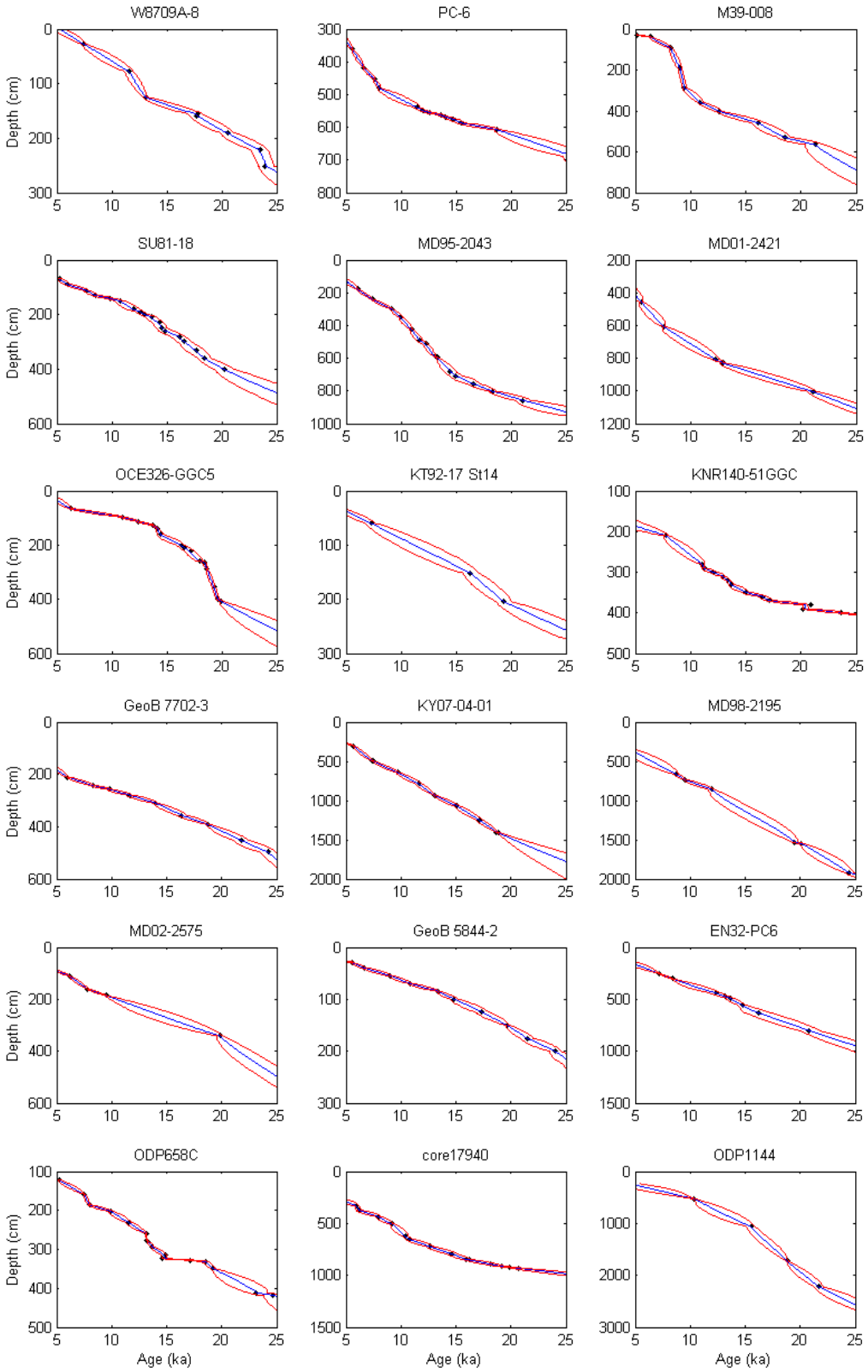

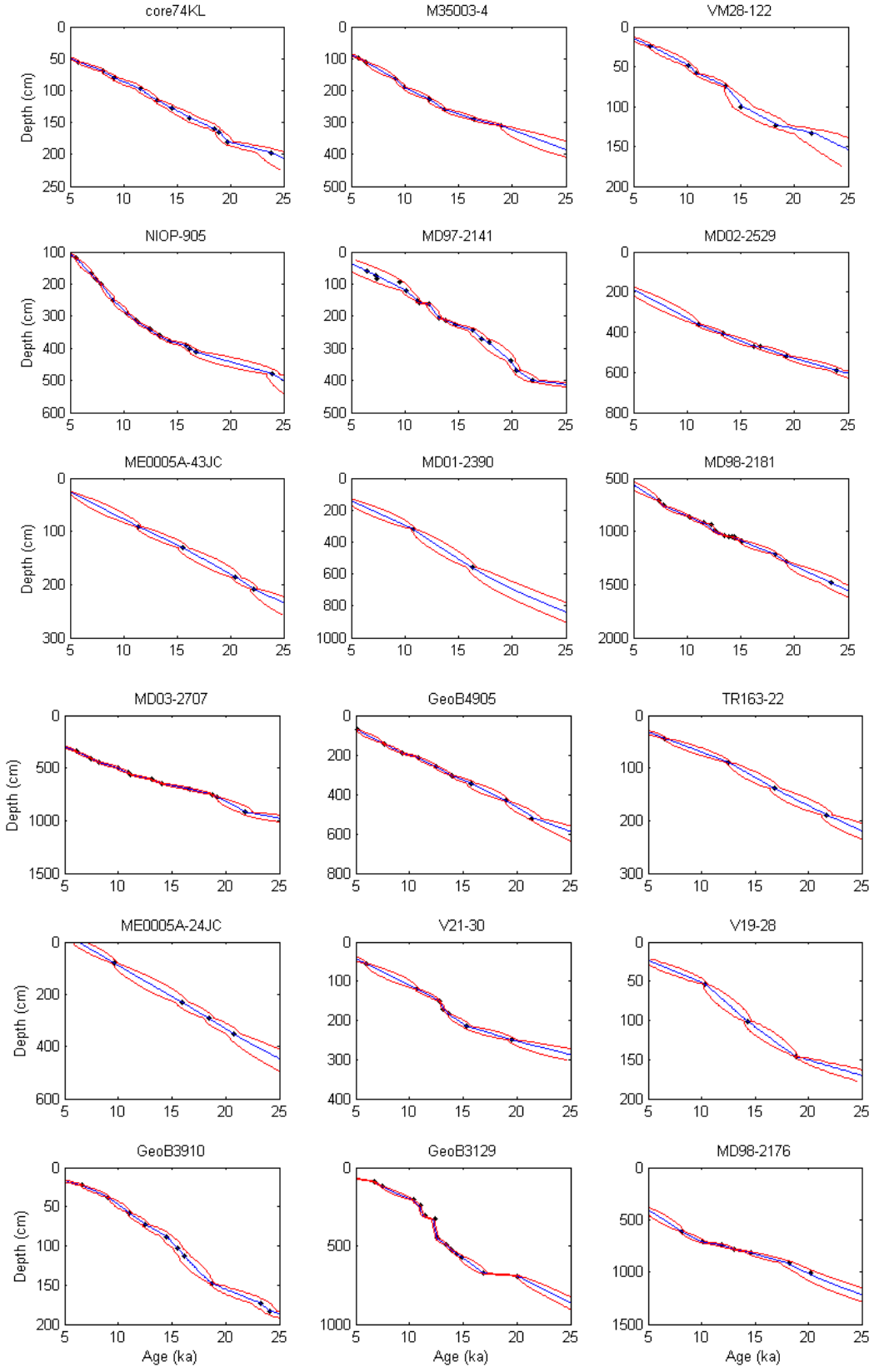
core74KL
M35003-4
VM28-122
NIOP-905
MD97-2141
MD02-2529
ME0005A-43JC
MD01-2390
MD98-2181
MD03-2707
GeoB4905
TR163-22
ME0005A-24JC
V21-30
V19-28
GeoB3910
GeoB3129
MD98-2176
Depth (cm)
Age (ka)

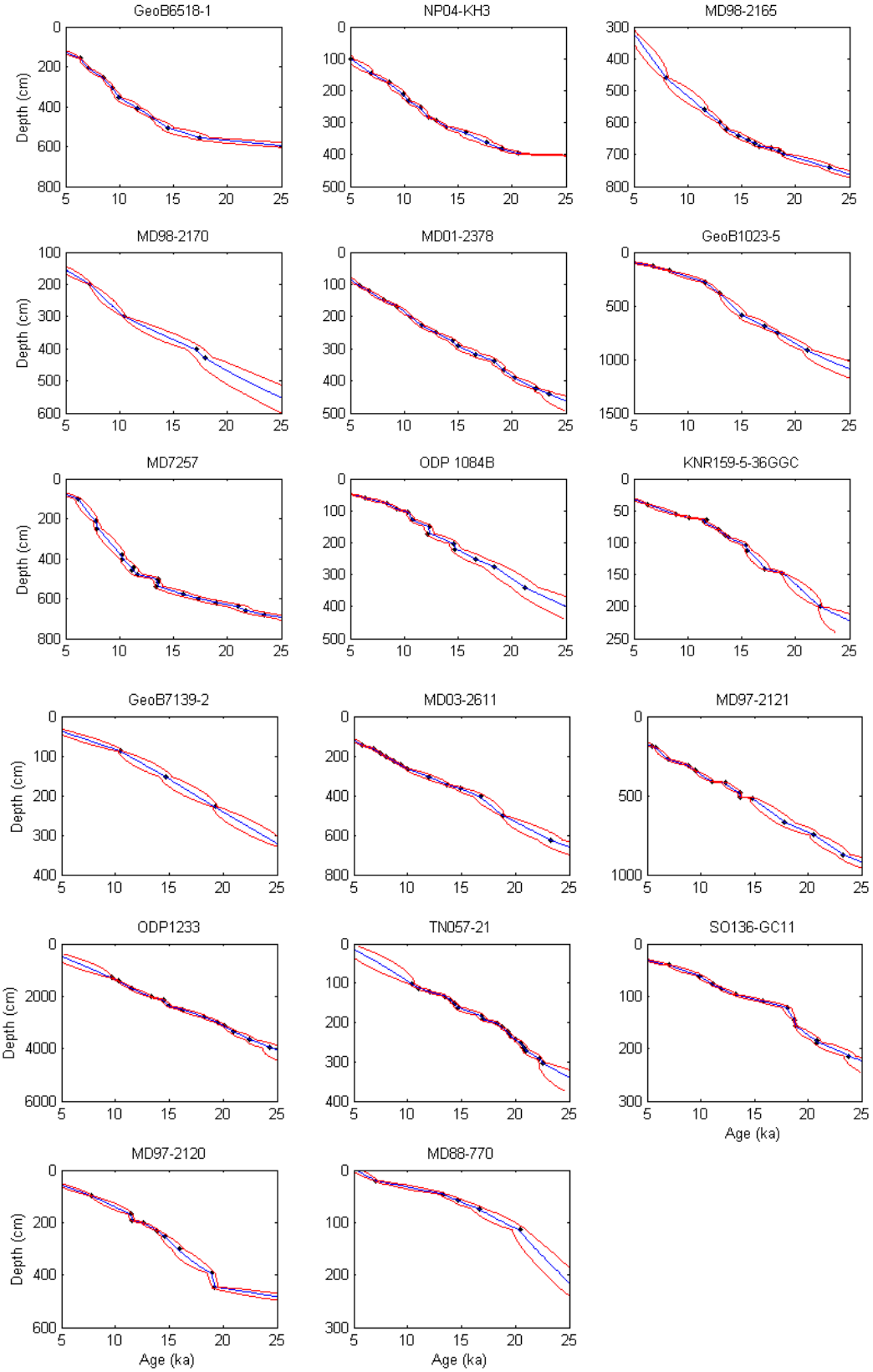
GeoB6518-1
NP04-KH3
MD98-2165
MD98-2170
MD01-2378
GeoB1023-5
MD7257
ODP 1084B
KNR159-5-36GGC
GeoB7139-2
MD03-2611
MD97-2121
ODP1233
TN057-21
SO136-GC11
MD97-2120
MD88-770
Depth (cm)
Age (ka)

Proxy temperature record plots: Proxy temperature records (blue) with 2σ uncertainties (red lines) reflecting both chronological and proxy calibration uncertainties.

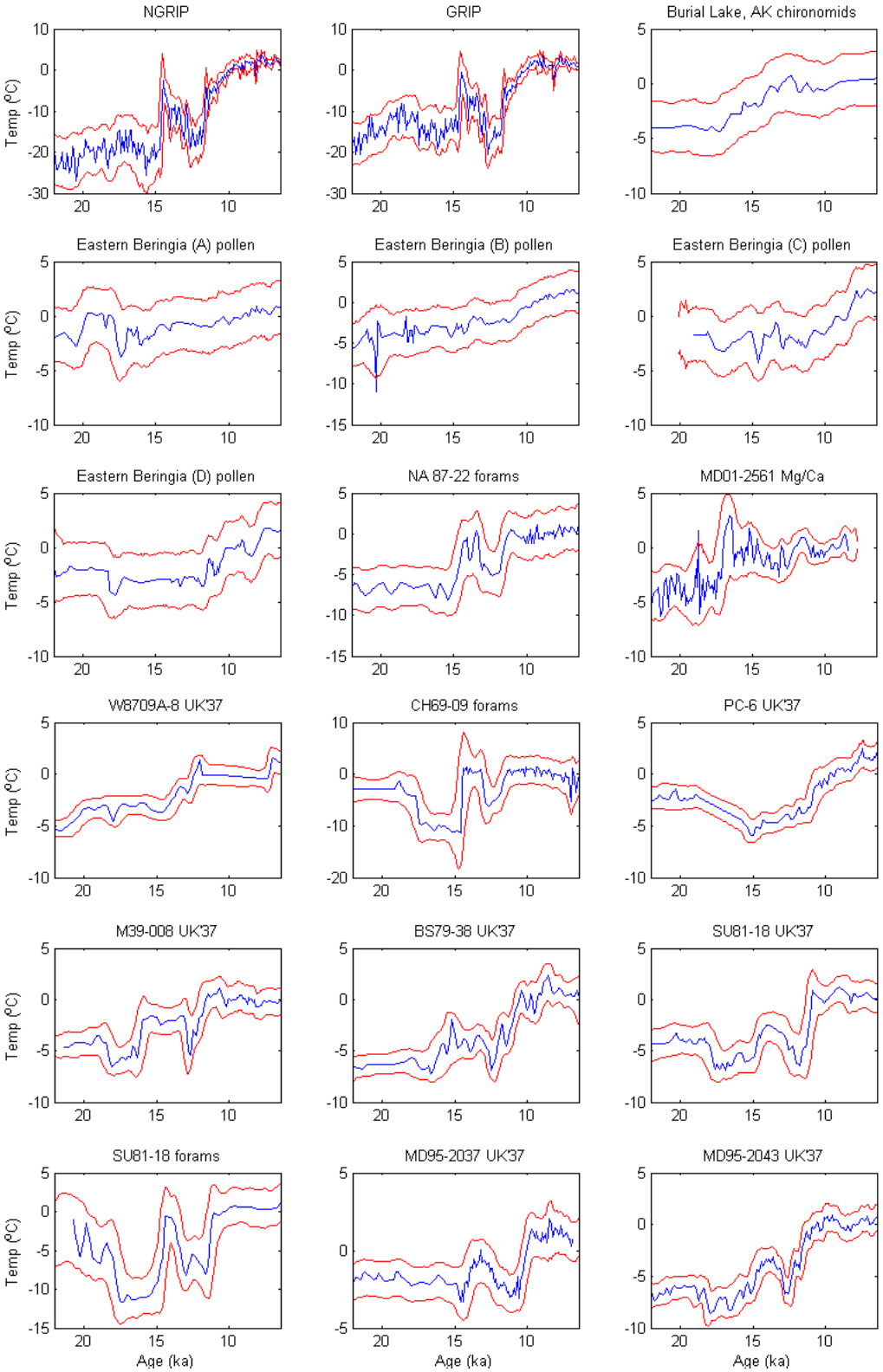

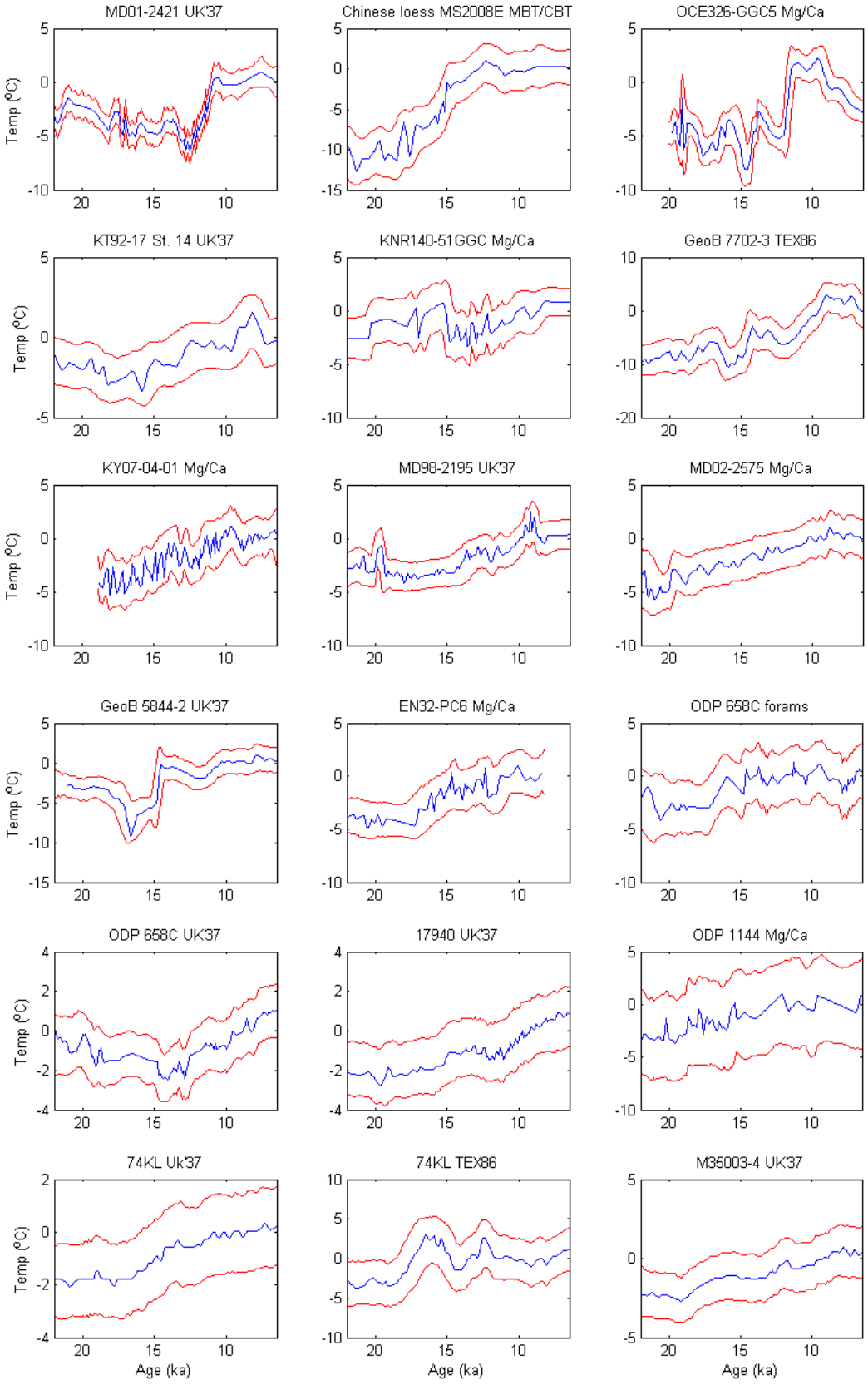
MD01-2421 UK'37
Chinese loess MS2008E MBT/CBT
OCE326-GGC5 Mg/Ca
KT92-17 St. 14 UK'37
KNR140-51GGC Mg/Ca
GeoB 7702-3 TEX86
KY07-04-01 Mg/Ca
MD98-2195 UK'37
MD02-2575 Mg/Ca
GeoB 5844-2 UK'37
EN32-PC6 Mg/Ca
ODP 658C forams
ODP 658C UK'37
17940 UK'37
ODP 1144 Mg/Ca
74KL Uk'37
74KL TEX86
M35003-4 UK'37
Temp (°C)
Age (ka)

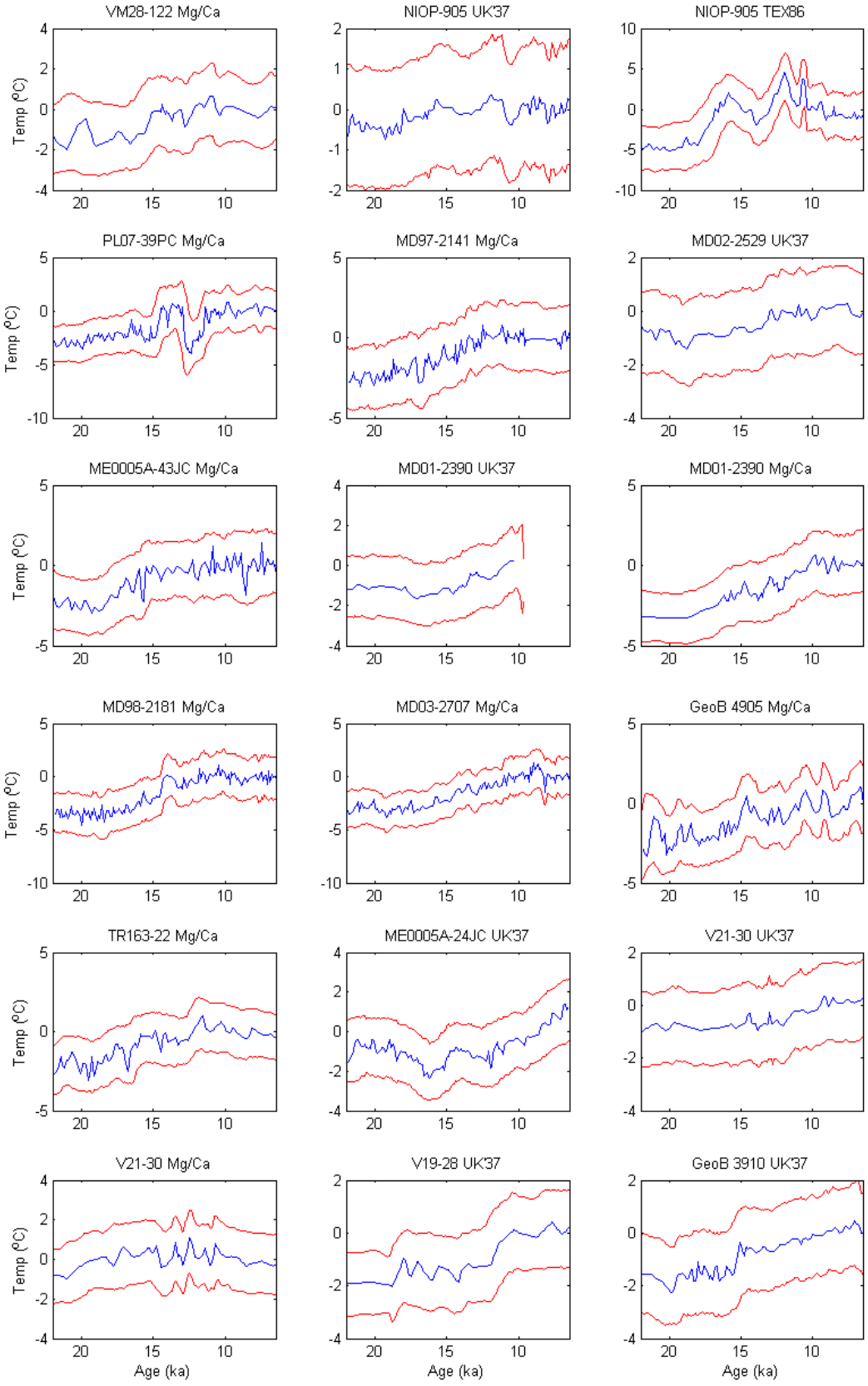
VM28-122 Mg/Ca
NIOP-905 UK'37
NIOP-905 TEX86
PL07-39PC Mg/Ca
MD97-2141 Mg/Ca
MD02-2529 UK'37
ME0005A-43JC Mg/Ca
MD01-2390 UK'37
MD01-2390 Mg/Ca
MD98-2181 Mg/Ca
MD03-2707 Mg/Ca
GeoB 4905 Mg/Ca
TR163-22 Mg/Ca
ME0005A-24JC UK'37
V21-30 UK'37
V21-30 Mg/Ca
V19-28 UK'37
GeoB 3910 UK'37
Temp (°C)
Age (ka)

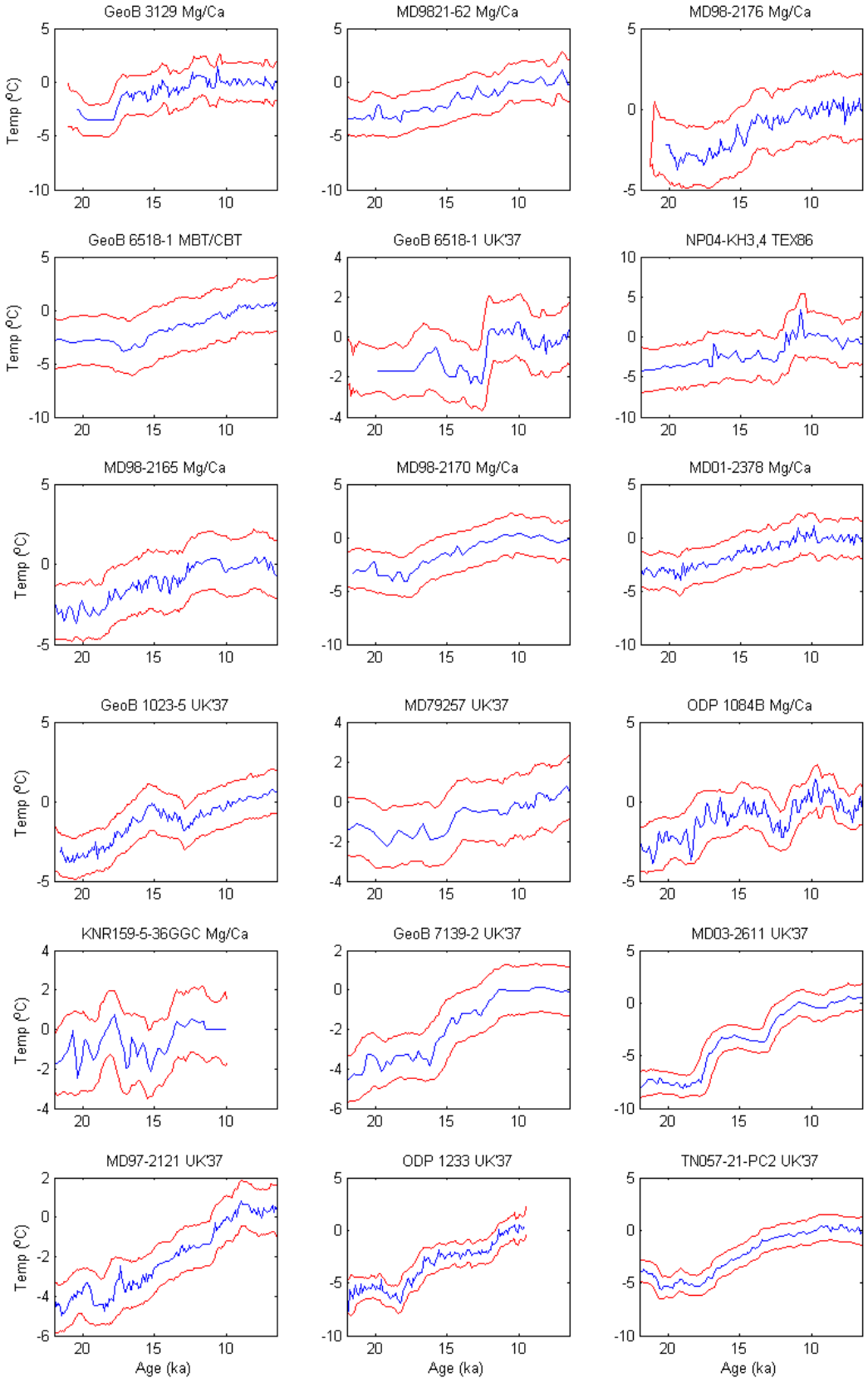
GeoB 3129 Mg/Ca
MD9821-62 Mg/Ca
MD98-2176 Mg/Ca
GeoB 6518-1 MBT/CBT
GeoB 6518-1 UK'37
NP04-KH3,4 TEX86
MD98-2165 Mg/Ca
MD98-2170 Mg/Ca
MD01-2378 Mg/Ca
GeoB 1023-5 UK'37
MD79257 UK'37
ODP 1084B Mg/Ca
KNR159-5-36GGC Mg/Ca
GeoB 7139-2 UK'37
MD03-2611 UK'37
MD97-2121 UK'37
ODP 1233 UK'37
TN057-21-PC2 UK'37
Temp (°C)
Age (ka)

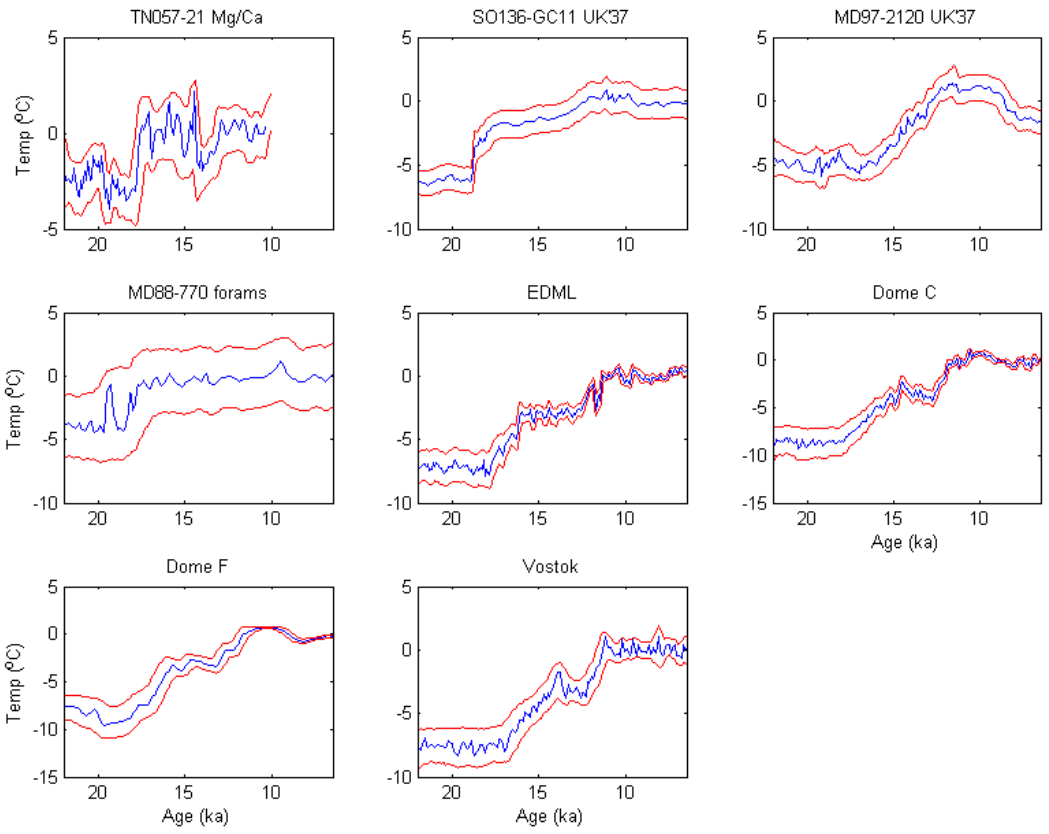
TN057-21 Mg/Ca
SO136-GC11 UK'37
MD97-2120 UK'37
MD88-770 forams
EDML
Dome C
Dome F
Vostok
Temp (°C)
Age (ka)